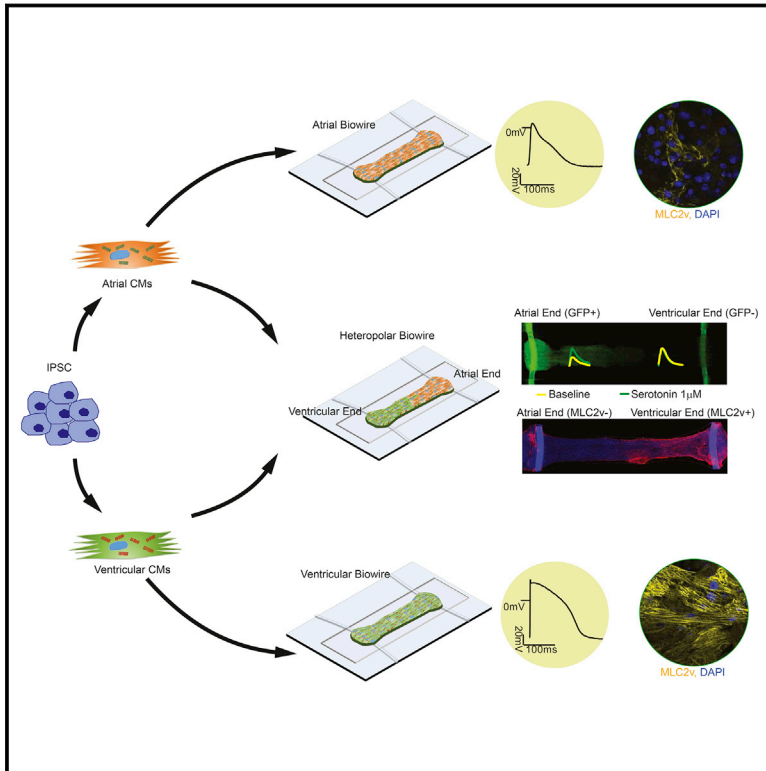


A Platform for Generation of Chamber-Specific Cardiac Tissues and Disease Modeling

Graphical Abstract



Authors

Yimu Zhao, Naimeh Rafatian, Nicole T. Feric, ..., Ulrich Broeckel, Peter H. Backx, Milica Radisic

Correspondence

p.backx@utoronto.ca (P.H.B.),
m.radisic@utoronto.ca (M.R.)

In Brief

A scalable cardiac tissue cultivation platform enables assessment of multiple parameters of atrial and ventricular tissue function, drug testing, and disease modeling.

Highlights

- Positive force frequency and post-rest potentiation are achieved in human tissues
- Engineered atrial and ventricular tissues have distinct electrophysiology and drug responses
- Atrio-ventricular tissues show spatially confined drug responses
- Long-term electrical conditioning enables polygenic cardiac disease modeling

A Platform for Generation of Chamber-Specific Cardiac Tissues and Disease Modeling

Yimu Zhao,¹ Naimeh Rafatian,² Nicole T. Feric,^{3,4} Brian J. Cox,^{5,6} Roozbeh Aschar-Sobbi,^{2,3} Erika Yan Wang,⁴ Praful Aggarwal,⁷ Boyang Zhang,^{1,4} Genevieve Conant,^{1,4} Kacey Ronaldson-Bouchard,^{3,8} Aric Pahnke,^{1,4} Stephanie Protze,^{9,10} Jee Hoon Lee,^{10,11} Locke Davenport Huyer,^{1,4} Danica Jekic,^{1,12} Anastasia Wickeler,¹³ Hani E. Naguib,¹³ Gordon M. Keller,¹⁰ Gordana Vunjak-Novakovic,⁸ Ulrich Broeckel,⁷ Peter H. Backx,^{2,5,14,15,*} and Milica Radisic^{1,4,15,16,*}

¹Department of Chemical Engineering and Applied Chemistry, University of Toronto, Toronto, ON M5S 3E5, Canada

²Division of Cardiology and Peter Munk Cardiac Center, University of Health Network; Toronto, ON M5G 2N2, Canada

³TARA Biosystems, Inc., New York, NY 10016, USA

⁴Institute of Biomaterials and Biomedical Engineering, University of Toronto, Toronto, ON M5S 3G9, Canada

⁵Department of Physiology, Faculty of Medicine; University of Toronto; Toronto; Ontario, M5S 1A8, Canada

⁶Department of Obstetrics and Gynaecology, Faculty of Medicine, University of Toronto, Toronto, ON M5S 1A8, Canada

⁷Section of Genomic Pediatrics, Department of Pediatrics and Genomic Sciences and Precision Medicine Center, Medical College of Wisconsin, Milwaukee, WI 53226, USA

⁸Department of Biomedical Engineering and Department of Medicine, Columbia University, New York, NY 10032, USA

⁹Department of Molecular Genetics, University of Toronto, Toronto, ON M5G 1A8, Canada

¹⁰McEwen Stem Cell Institute, University Health Network, Toronto, ON M5G 1L7, Canada

¹¹BlueRock Therapeutics, MaRS Discovery District, Toronto, ON M5G 1L7, Canada

¹²Department of Anatomy and Cell Biology, Faculty of Science, McGill University, Montreal, QC H3A 2K6, Canada

¹³Department of Mechanical and Industrial Engineering, University of Toronto, Toronto, ON M5S 3G8, Canada

¹⁴Department of Biology; York University, Toronto, ON M3J 1P3, Canada

¹⁵Toronto General Hospital Research Institute, Toronto, ON M5G 2C4, Canada

¹⁶Lead Contact

*Correspondence: p.backx@utoronto.ca (P.H.B.), m.radisic@utoronto.ca (M.R.)

<https://doi.org/10.1016/j.cell.2018.11.042>

SUMMARY

Tissue engineering using cardiomyocytes derived from human pluripotent stem cells holds a promise to revolutionize drug discovery, but only if limitations related to cardiac chamber specification and platform versatility can be overcome. We describe here a scalable tissue-cultivation platform that is cell source agnostic and enables drug testing under electrical pacing. The plastic platform enabled on-line noninvasive recording of passive tension, active force, contractile dynamics, and Ca^{2+} transients, as well as endpoint assessments of action potentials and conduction velocity. By combining directed cell differentiation with electrical field conditioning, we engineered electrophysiologically distinct atrial and ventricular tissues with chamber-specific drug responses and gene expression. We report, for the first time, engineering of heteropolar cardiac tissues containing distinct atrial and ventricular ends, and we demonstrate their spatially confined responses to serotonin and ranolazine. Uniquely, electrical conditioning for up to 8 months enabled modeling of polygenic left ventricular hypertrophy starting from patient cells.

INTRODUCTION

Profound physiological differences among species—in action potentials, ion current profiles, and contractile rates—motivate the development of human cardiac tissues for drug testing and disease modeling. Although ideal platforms should yield distinct atrial and ventricular tissues, most approaches using human pluripotent stem cells (hPSC) have focused on generating ventricular myocardium (Ahn et al., 2018; Eschenhagen et al., 2012; Lemoine et al., 2017; Lind et al., 2017a; MacQueen et al., 2018; Nunes et al., 2013; Schaaf et al., 2011; Tulloch et al., 2011); (Lemoine et al., 2018; Lind et al., 2017b; Tiburcy et al., 2017) and assessing adverse ventricular events (Vicente et al., 2015). This has been in part due to the lag in developing reliable chamber-specific hPSC differentiation protocols (Cyganek et al., 2018; Lee et al., 2017). Screening for atrial toxicity is critical, given that atrial and ventricular cardiomyocytes (CMs) have distinct properties (Grandi et al., 2011). The ventricles and atria have unique chamber-specific defects and drug-induced myopathies (van der Hooft et al., 2004), making human ventricular myocardium an inadequate platform for discovery of atrial drugs. The atrial-specific platforms are especially important, given that atrial fibrillation is the most common cardiac arrhythmia, for which current treatment approaches have limited success (Chen et al., 2013; Eisen et al., 2016). Currently used pharmacological agents for treating atrial fibrillation have deadly unwanted side-effects on ventricular CMs which predispose to sudden cardiac death.

Induced pluripotent stem cells (iPSC) offer the possibility to determine the pathogenesis of cardiac disease as demonstrated with cardiac microtissues used to model cardiomyopathy as a result of sarcomeric protein titin truncations (Hinson et al., 2015) or mitochondrial protein tafazzin mutations (Wang et al., 2014). However, some of the most common cardiac diseases are complex, polygenic conditions that are strongly influenced by environmental factors. For example, prolonged hypertension leads to cardiac hypertrophy, left ventricular dysfunction, and ultimately heart failure. Thus, to model polygenic disease, it is critical to provide a chronic increased workload to the cardiac tissue over a prolonged period.

Our goal was to develop a versatile resource for the community, a platform that enables creation of electrophysiologically distinct atrial and ventricular tissues, that is capable of providing months long biophysical stimulation of 3D tissues to model a polygenic disease. This platform, termed Biowire II, enables growth of thin, cylindrical tissues, like human trabeculae, suspended between two parallel wires that allow simultaneous quantification of force and Ca^{2+} transients. Using directed differentiation protocols and electrical conditioning, atrial versus ventricular specification is robustly achieved. We demonstrate the utility of the described resource by constructing ventricular tissues from 6 healthy hPSC lines and 6 iPSC lines derived from patients with prolonged hypertension, as well as atrial tissues from 2 healthy hPSC lines. We also performed drug testing with heteropolar biowires constructed with distinct atrial and ventricular ends.

RESULTS

Generating Heart Tissues from Multiple Cell Sources

Figure 1A and Figure S1A illustrate the general features of our “Biowire” platform, which consists of an array of microwells (5 mm × 1 mm × 0.3 mm) patterned onto polystyrene sheets. Two flexible wires fabricated from a poly(octamethylene maleate (anhydride) citrate) (POMaC) polymer are secured with adhesive glue along either end of the microwells. Myocardial tissues are created by combining CMs (either ventricular or atrial or both) and cardiac fibroblasts (usually at a 10:1 ratio) with hydrogel within the microwells. During the next 7 days, cells undergo “compaction”, thereby forming cylindrical trabecular strips (called Biowires II) that are suspended in the microwell but physically attached to the POMaC wires (Figures S1A, S1C, and S1D; Video S1). Beginning at 1 week, the suspended tissues are electrically conditioned for weeks with electrical field stimulation via a pair of carbon electrodes connected to a stimulator with platinum wires (Figure S1A).

A typical biowire created using ventricular CMs from BJ1D stem cells displays uniform longitudinal alignment of sarcomeric contractile proteins (Figures 1C and 1D) after 6 weeks in culture. Additional examples of biowires using CMs obtained from other stem cell sources are presented in Figure 1E while Figure S1B lists all the sources of cells used in our studies.

Biowire II Platform Exhibits Reduced Absorption of Hydrophobic Compounds

Most previous 3D cell cultivation platforms have used materials such as polydimethylsiloxane (PDMS) (Huebsch et al., 2016; Ma-

thur et al., 2015; Nunes et al., 2013; Sidorov et al., 2017; Wang et al., 2014; Hinson et al., 2015), which absorb hydrophobic drugs (Toepke and Beebe, 2006) thereby complicating the interpretation of both long-term and short-term drug screening studies. We found that although the fluorescence levels of moderately hydrophobic compound Rhodamine B declined with time in our biowire chips, they nevertheless remained higher than in PDMS chips when incubation times were 24 h and longer (Figure 1F). Moreover, after 6 h, the levels of Rhodamine B were not significantly different compared to the tissue plastic well controls. Similarly, the levels of a more hydrophobic compound (Rhodamine 6G) were also higher in our biowire chips ($6.8 \pm 0.9\text{nM}$) compared to PDMS chips ($5.4 \pm 0.5\text{nM}$, $p = 0.0109$) when incubation times were reduced to 30 min, indicating less absorption by the biowire chip compared to the PDMS chip in an acute test. The time-dependent reductions in Rhodamine B were associated with the appearance of rhodamine fluorescence throughout the PDMS chips, whereas the fluorescence in our biowire chips was limited to the POMaC wires. After extensive washout for 2 h, the fluorescence remained widespread in the PDMS chips while being undetectable in the biowire chips (Figure 1G).

Stable Non-invasive Force Recordings in Biowires

Because biowires attach to the elastic POMaC wires at the ends of the microwells, it becomes possible to non-invasively estimate the forces generated by biowires in response to contraction throughout the culture period by assessing the bonding properties of the POMaC wires (Video S2). For calibration, we displaced POMaC wires at their centers (Figures 2A and 2B). We found that, regardless of the probe cross-sectional area, POMaC wires reproducibly displayed non-linear elastic behavior over the range of wire displacements typically produced by biowire tissues (Figure S1E–S1J). These elastic properties of the POMaC wires could be readily modeled using finite element analysis (Figures S1H and S1I). Importantly, the force-displacement curves were unaltered after 6 weeks in culture (Figure 2C), and the Young’s Modulus estimates of the POMaC wires remained unchanged for up to 3 months in culture (Figure 2D).

To assess the passive and active forces generated by the biowires, we took advantage of the intrinsic fluorescence of POMaC wires when illuminated with blue light ($\lambda_{\text{ex}}350\text{ nm}/\lambda_{\text{em}}470\text{ nm}$). Fluorescence imaging of ventricular biowires during electrical pacing (Figure 2E) revealed that the POMaC wires are typically bent somewhat at baseline, indicating passive tension, and undergo dynamic time-dependent deformations arising from active force generation. Conversion of the wire deformations into force, via our calibration curves, allows for non-invasive estimation of force properties (i.e., resting tension, active force, rates of force development, and relaxation) throughout the culture period (Figure 2F).

To illustrate the utility of dynamic force recordings, we examined the effects of several agents with known cardiac effects in ventricular biowires, created from BJ1D iPSCs and HES3 ESCs (Figure 2G). The results reveal that: the β -adrenoceptor agonist, isoproterenol, increases contractility; the L-type calcium channel blocker, diltiazem, produces negative inotropic effects; the sodium channel blocker, lidocaine, inhibits tissue

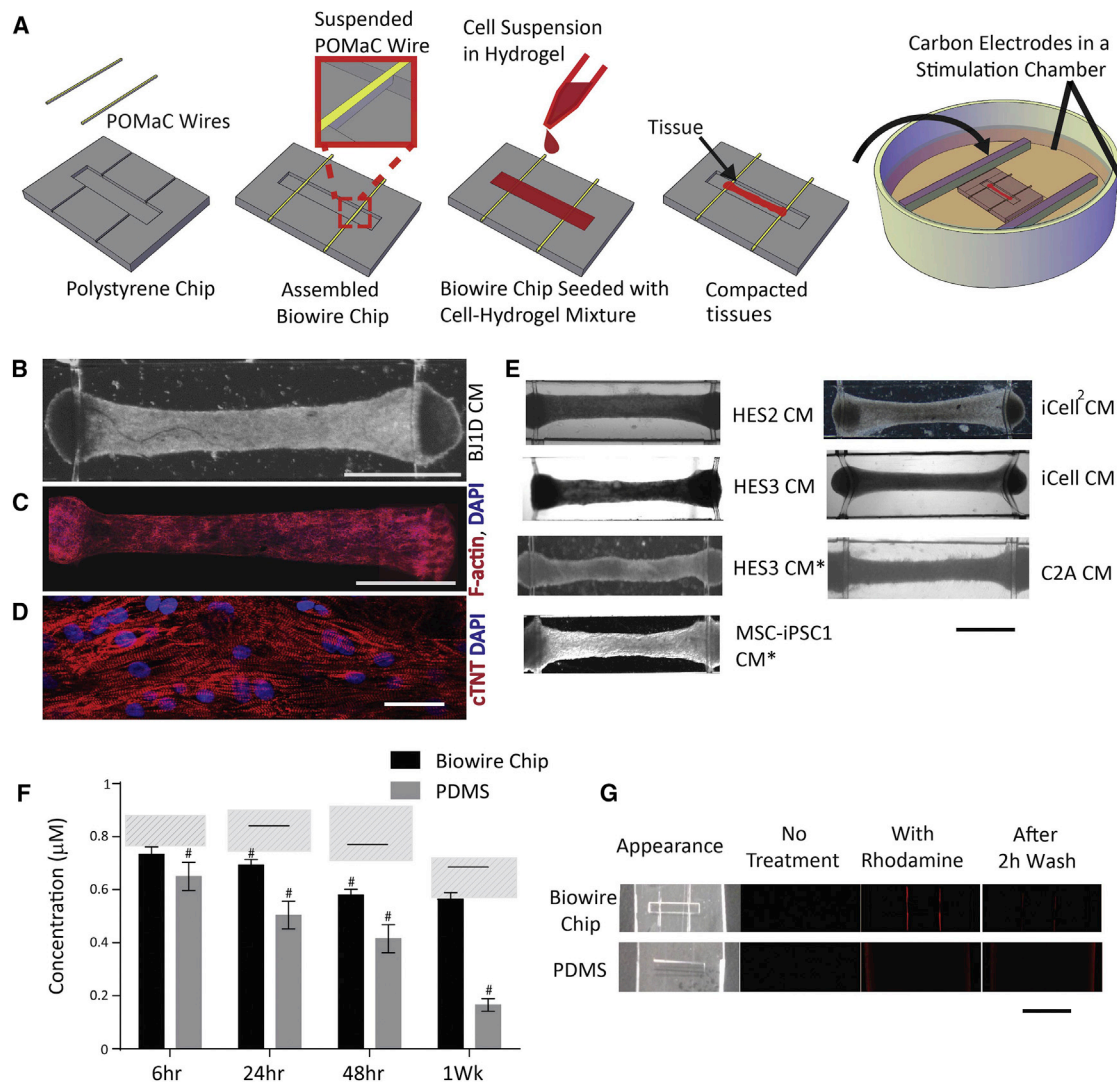


Figure 1. The Biowire II Platform for Micro-scale Engineered Cardiac Tissues

(A–D) (A) Schematic. Representative tissues in Biowire II platform: (B) bright field image (Scale bar, 1mm); composite confocal images of (C) F-actin and DAPI staining (Scale bar, 1mm) and (D) troponin-T and DAPI staining (Scale bar, 30 μ m).

(E) Representative bright field images of tissues from several CM sources; asterisk (*) denotes atrial-specific tissues. (Scale bar, 1mm).

(F) Rhodamine B absorption after incubation in Biowire II or PDMS chips for 6 h, 24 h, 48 h, and 1 week. # indicates $p < 0.05$ versus control at each time point. Solid line indicates significant difference between the two groups. Dashed areas represent levels of rhodamine B in control polystyrene tissue culture wells. (Data shown as avg \pm stdev, $n = 3$, Two-way ANOVA plus Tukey's test).

(G) Bright field and fluorescence images of chips without rhodamine B incubation (no treatment), incubated with rhodamine B for 1 week (with rhodamine) and incubated with rhodamine B for 1 week followed by washout for 2 h (after 2 h wash). Scale bar, 5mm.

See also [Figure S1](#) and [Video S1](#).

electrical excitability; the cAMP phosphodiesterase 3 inhibitor, milrinone, enhances contractility and the human ether-a-go-go (hERG) channel blocker, E-4031, promotes spontaneous irregular beating patterns consistent with arrhythmias ([Figure 2G](#)).

Generating Atrial and Ventricular Biowires

Biowires generated using directed differentiation protocols designed to produce either atrial or ventricular CMs ([Lee et al., 2017](#); [Lian et al., 2012](#)) revealed that both types of tissues underwent similar cellular compaction over the first 7 days in culture

([Figure S2A](#)). CMs appeared to occupy the majority of tissue volume ([Figure S2F](#)) as in the native myocardium for both types of biowires. After compaction, biowires were routinely conditioned using chronic electrical stimulation protocols ([Figure 3A](#)) with stimulation rates that were progressively increased over time, in order to promote cardiac maturation, as shown previously ([Nunes et al., 2013](#); [Ronaldson-Bouchard et al., 2018](#)). Consistent with shorter refractoriness in atrial myocardium, maximum stimulation rates could be achieved more rapidly in atrial versus ventricular biowires ([Figure 3A](#)).

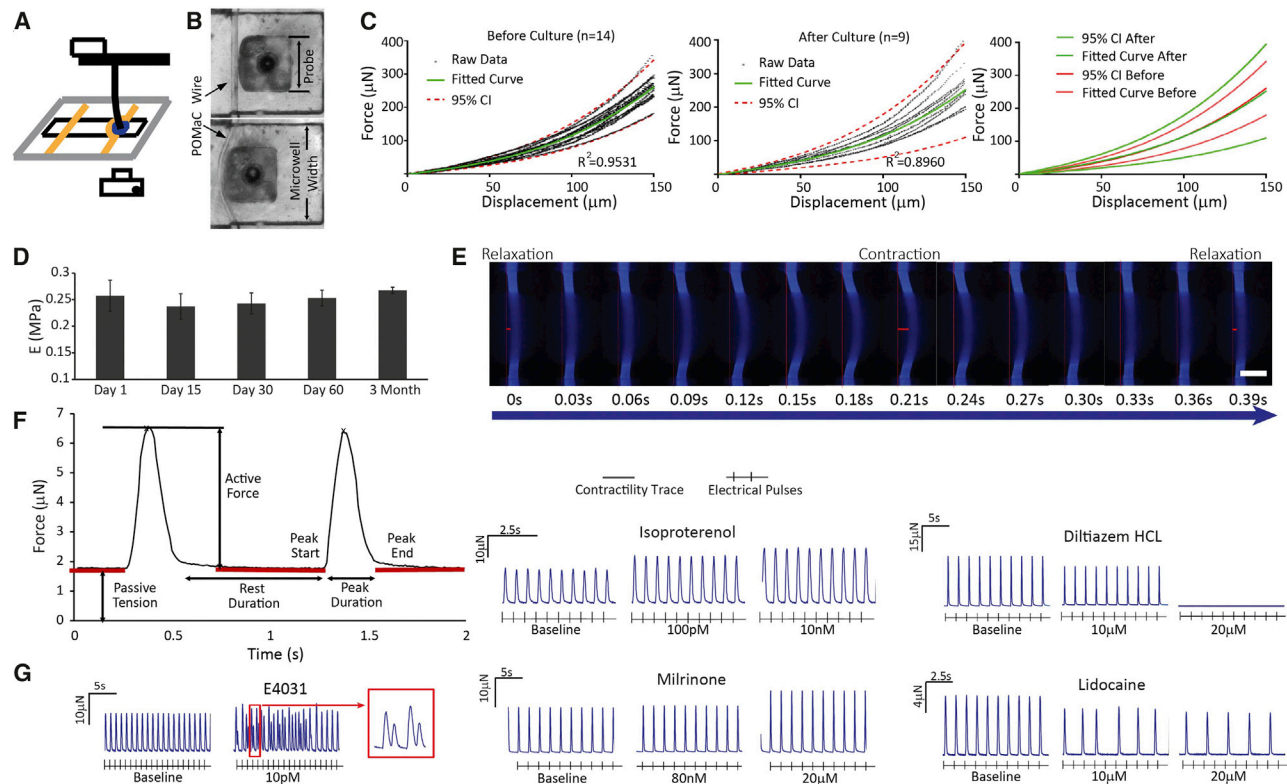


Figure 2. Biowire II Platform Enables Non-invasive Assessment of Passive Tension and Active Force

(A) Schematic of apparatus for calibrating POMaC wires using a displacement test.

(B) POMaC wire configuration prior to contact and after displacement by a 0.5 mm probe.

(C) No differences in mechanical properties of the POMaC wires were detected before and 6 weeks after cell cultivation.

(D) The Young's Modulus of POMaC wires was comparable during 3 months of culture with cells and media (avg \pm stdev, $n \geq 3$, one-way ANOVA).

(E) Time lapse images showing POMaC wire bending by tissue contraction, paced at 1 Hz. Scale bar, 200 μ m. Wire bending due to passive tension and active force are illustrated by the red bars.

(F) Typical force traces of contracting tissues.

(G) Representative traces of changes in active force and beat patterns of tissues under stimulation in response to the application of compounds with well-known cardiac actions. Tissues were generated from ventricular Hes3 hESC-CM and BJ1D iPSC-CM.

See also [Figure S1](#) and [Video S2](#).

Principal component analyses (PCA) of RNA sequencing data (63,967 genes) (NCBI: GSE114976), after removal of low expressed genes (17620 genes), revealed strongly enhanced atrial or ventricular identities in response to electrical conditioning. Specifically, the first component of the PCA ([Figure 3B](#)), which accounted for >50% of the variance in gene expression, segregated atrial from ventricular tissues. The second PCA component (28% of variance) separated stimulated and unstimulated ventricular tissues, while the third component (6% of variance) separated the stimulated and unstimulated atrial tissues. This indicates that the most profound changes due to electrical conditioning were to the ventricle samples and that the gene expression changes induced in the atrial and ventricular cells by stimulation were independent ([Figure 3B](#)).

Gene set enrichment analyses (GSEA) and manual curation of the clear transcriptional distinction between atrial and ventricular biowires, with and without electrical conditioning, identified changes in known markers of cardiac chambers, metabolic, and structural gene sets needed for adult heart function ([Figures](#)

[S3A–S3D](#)). Known atrial and atrial-enriched markers ([Figure 3C](#)) such as *NPPA*, *GJA5*, *KCNJ12*, *MYH6*, and *MYL4* ([Gaborit et al., 2007](#), [Asp et al., 2012](#)) were expressed at higher levels in atrial compared to the ventricular biowires.

We found that electrically conditioned biowires were enriched for gene expression patterns of the corresponding adult human heart cardiac regions ([Figure 3D](#)). Consistent with these results, histological analyses demonstrate that electrical conditioning improves sarcomeric organization for both atrial and ventricular biowires ([Figures 3E, 3F, and S2D](#)) while also clearly promoting the expression of maturation genes in ventricular biowires associated with contraction, Ca^{2+} handling and electrical properties ([Figures 3C and S3A](#)), and lipid metabolism ([Figure S3B](#)).

Consistent with adult human atrial muscle ([Iwashiro et al., 1997](#)), the atrial biowires display a relatively flat force-frequency relationship (FFR) with no appreciable post-rest potentiation (PRP) of force regardless of electrical conditioning, although normalized force amplitudes, measured with 3Hz pacing, are about ~30% larger in conditioned atrial biowires compared

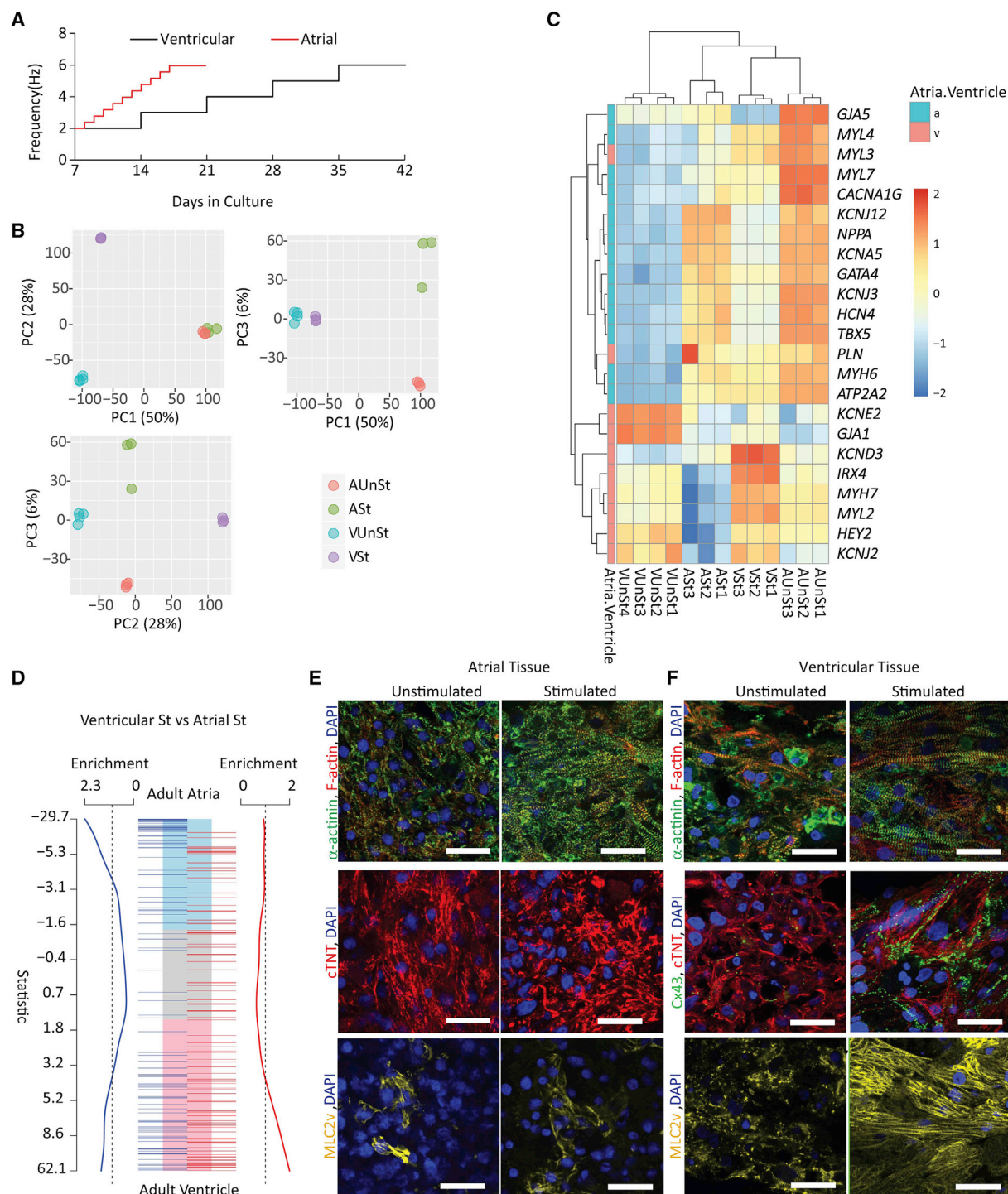


Figure 3. Atrial and Ventricular Tissues Exhibit Distinct Patterns of Gene Expression and Morphology upon Chronic Electrical Conditioning

(A) Electrical conditioning protocols. (B) Principal component analyses indicate distinct clustering of atrial versus ventricular tissues with (St) and without (UnSt) electrical conditioning (n = 3–4/group). (C) Heatmaps illustrating differences in expression levels of selected atrial and ventricular functional markers. (D) Gene set enrichments based on custom cardiac ontologies for adult ventricle and atria. Electrically conditioned ventricular biowires are significantly enriched for human ventricular genes, whereas conditioned atrial biowires are enriched for human atrial genes. In (A)–(D), all tissues were derived from HES3 cells.

(legend continued on next page)

to the control atrial biowires (Figures 4A, 4B, and 4D). By contrast, electrical conditioning of ventricular biowires increases ($p < 0.0001$) contractile amplitudes, converts the FFR profiles from flat to positive ($p < 0.0001$) (Figure S4A), and produces prominent PRP of force in ventricular tissues, as seen in adult human ventricles (Figures 4A, 4C, and 4D). Specifically, post-rest force after pacing at 6 Hz was ~ 2.5 -fold higher ($p = 0.044$) than the force at 6 Hz pacing (Figure 4D) and was ~ 21 -fold higher ($p < 0.0001$) than the force measured at 1 Hz. It is notable that atrial biowires generate less force than ventricular biowires (Figure 4A), as expected from the lower contractile protein densities in atrial versus ventricular biowires seen with histology (Figures 3E and 3F).

The electrical properties of biowires also show distinct tissue specification. With time in culture, the excitation threshold voltage (ET) needed to initiate contraction decreased, while the maximum capture rates (MCR) increased for both atrial and ventricular biowires (Figures S2B and S2C). Moreover, conditioning had no effect ($p = 0.9830$) on conduction velocities (CVs) in atrial (HES3 hESC-CM) tissues (5.6 ± 1.0 cm/s without versus 5.7 ± 0.9 cm/s with conditioning) while increasing ($p = 0.0286$) CV from 13.0 ± 5.5 cm/s to 31.8 ± 7.9 cm/s in ventricular (BJ1D iPSC) biowires (Figure 4 E and 4F, Videos S3 and S4). Similarly, electrical conditioning of atrial biowires has minimal effects on action potential (AP) properties, while altering most AP parameters (except MDP and APD₉₀) in ventricular tissues (Figures 4G–4M). Of particular note, electrically conditioned ventricular tissues possess rapid upstroke velocities and display an early repolarization notch (Figure 4H), as seen in adult human epimyocardium that is linked to developmentally regulated transient outward K⁺ currents (Figures 4H and 4K) (Oudit et al., 2001).

Consistent with electrical differences between atrial and ventricular myocardium, the AP profiles in atrial tissues are distinctly different from ventricular tissues (Figure 4I–4M). Of particular note, the APD₃₀/APD₉₀ ratio, which is a distinguishing feature between atrial and ventricular CMs, was 0.45 ± 0.04 for ventricular tissues while being only 0.14 ± 0.04 for atrial tissues, similar to human myocardium (~ 0.75 for ventricular versus ~ 0.1 for atrial CMs) (Dawodu et al., 1996; O'Hara et al., 2011).

The biowires showed a high degree of reproducibility in passive tension, active force amplitudes, PRP, MCRs, and ETs between batches of conditioned ventricular tissues generated from BJ1D cells (Figures S4B–S4F), as well as with different stem cell sources. For example, while the genetic, structural, and functional results described above were recorded in atrial biowires generated from HES3 stem cells and in ventricular biowires created from BJ1D cells, conditioned ventricular biowires generated from HES3, and HES2 CMs exhibit similar positive FFR and undergo similar remodeling with electrical conditioning (Figures S4G–S4N). However, some baseline variability exists between biowires generated from different cell sources, HES3, iCell, and BJ1D stem cells (Figures S5A–S5D) in upstroke velocities and impulse propagation velocities which were lower ($p < 0.0001$ and

$p = 0.0095$) in HES3 derived biowires (i.e., 25.3 ± 14.0 mV/s and 5.7 ± 0.9 cm/s) than in BJ1D-derived biowires (108.8 ± 19.6 mV/s and 31.8 ± 7.9 cm/s). These differences can be explained by the higher MDP in HES3 biowires, which is expected to reduce Na⁺ channel availability via channel inactivation. Likewise, conditioned atrial biowires derived from different stem cells source (i.e., HES3 and MSC-IPS1) also produced relatively similar electrical properties (Figure S6). Importantly, standard pharmaceutical agents such as blockers of L-type Ca²⁺ channels (verapamil) and hERG channels (dofetilide) exhibited predictable responses on APs of ventricular biowires, (Figures S5E–S5N), thus further establishing their utility in drug testing.

Responses of Atrial versus Ventricular Tissues to Agents Affecting Functional Properties

Incubation of biowires with fluorescent Ca²⁺ indicators allows the simultaneous measurement of force and Ca²⁺ in our platform (Figures 5A and 5B; Video S5 and S6), thereby providing opportunities for convenient drug screening. To illustrate this capability (Figures 5C and 5D), we applied the L-type Ca⁺ channel blocker, nifedipine, which dose-dependently reduced force and Ca²⁺ transients with similar IC₅₀s in atrial biowires (IC₅₀ = 2.0 ± 1.2 μ M for force and 3.6 ± 1.5 μ M for Ca²⁺ transients) versus ventricular biowires (IC₅₀ = 4.5 ± 1.4 μ M for force and 3.1 ± 1.9 μ M for Ca²⁺ transients). Similarly, the sarco/endoplasmic reticulum calcium ATPase (SERCA) inhibitor, thapsigargin, dose-dependently decreased force and Ca²⁺ transient amplitudes (Figures 5E and 5F) in both atrial and ventricular preparations with higher potency in the ventricle, as expected with SERCA2a inhibition (Davia et al., 1997). Moreover, at low pacing rates, thapsigargin prolonged the time-to-peak and decay rates of both force and Ca²⁺ in ventricular, but not atrial biowires, consistent with differences in sarcoplasmic reticular Ca²⁺ handling between atrial and ventricular human myocardium (Blatter, 2017).

As expected (Zang et al., 2005), acetylcholine-dependent K⁺ currents (i.e., $I_{K,ACH}$) induced by the type 2 muscarinic receptor agonist, carbachol, abbreviated APDs in atrial biowires without affecting these parameters in ventricular tissues (Figures S7A–S7H). Another notable difference between atrial and ventricular myocardium is the presence in atria of K_v1.5-dependent ultra-rapidly activated potassium currents, I_{Kur} , a current with a high sensitivity to block by 4-aminopyridine (4AP) (Burashnikov and Antzelevitch, 2008). Accordingly, 4AP at low doses (25 μ M) increased AP amplitudes and prolonged APD₃₀ in the atrial biowires, without measurable effects on ventricular tissues (Figures S7I–S7P), although higher doses of 4AP did prolong APD, which may arise from blockade of the 4AP-sensitive Kv1.4-based transient outward currents (I_{to}) found in ventricular myocardium (Castle and Slawsky, 1993; Li et al., 1995).

In Vitro Disease Modeling Using the Biowire Platform

To demonstrate proof-of-concept for the utility of our biowire platform in disease modeling (Figure 6), iPSCs were obtained

(E and F) Confocal images of representative (E) atrial and (F) ventricular tissues immunostained for sarcomeric α -actinin and F-actin (first row); connexin-43 (Cx43, only for ventricular tissues) and cardiac troponin-T (second row) and Myosin light chain 2v (MLC2v) (third row). All samples were counterstained with DAPI. Atrial tissues were derived from HES3 hESC-CM and ventricular from BJ1D iPSC-CM. Scale bars, 30 μ m. See also Figure S3 and S4.

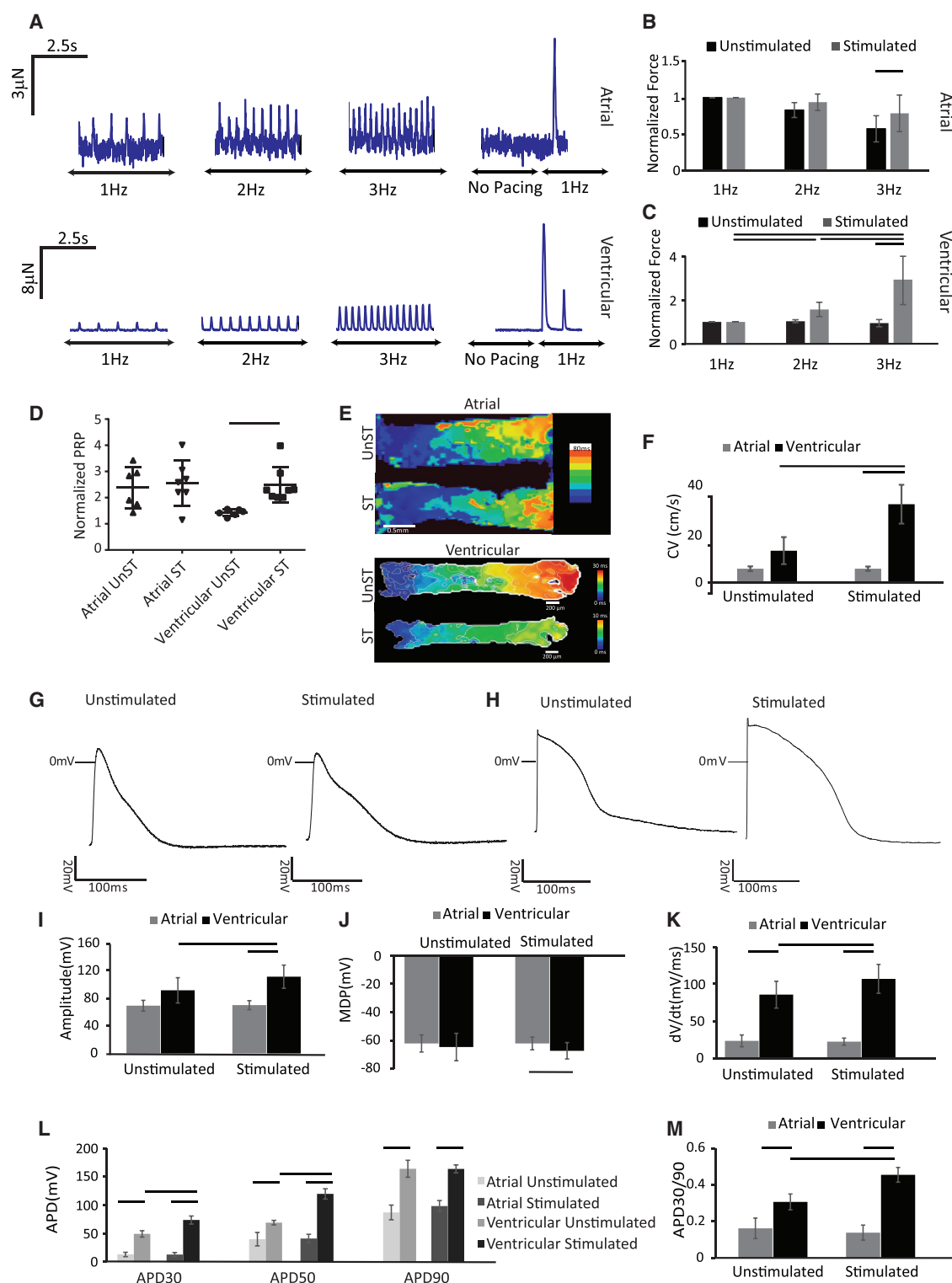


Figure 4. Atrial and Ventricular Tissues Exhibit Distinct Functional Responses after Electrical Conditioning

(A–C) (A) Representative force traces of atrial and ventricular tissues. Summary of active forces normalized to the force at 1 Hz for (B) atrial and (C) ventricular tissues with and without electrical conditioning (avg ± stdev, $n \geq 7$ for atrial and $n \geq 10$ for ventricular biowires, $p < 0.05$ with ANOVA on ranks and Mann-Whitney test).

(D) Summary results for PRP normalized to the last pacing frequency ($n \geq 6$, one-way ANOVA).

(legend continued on next page)

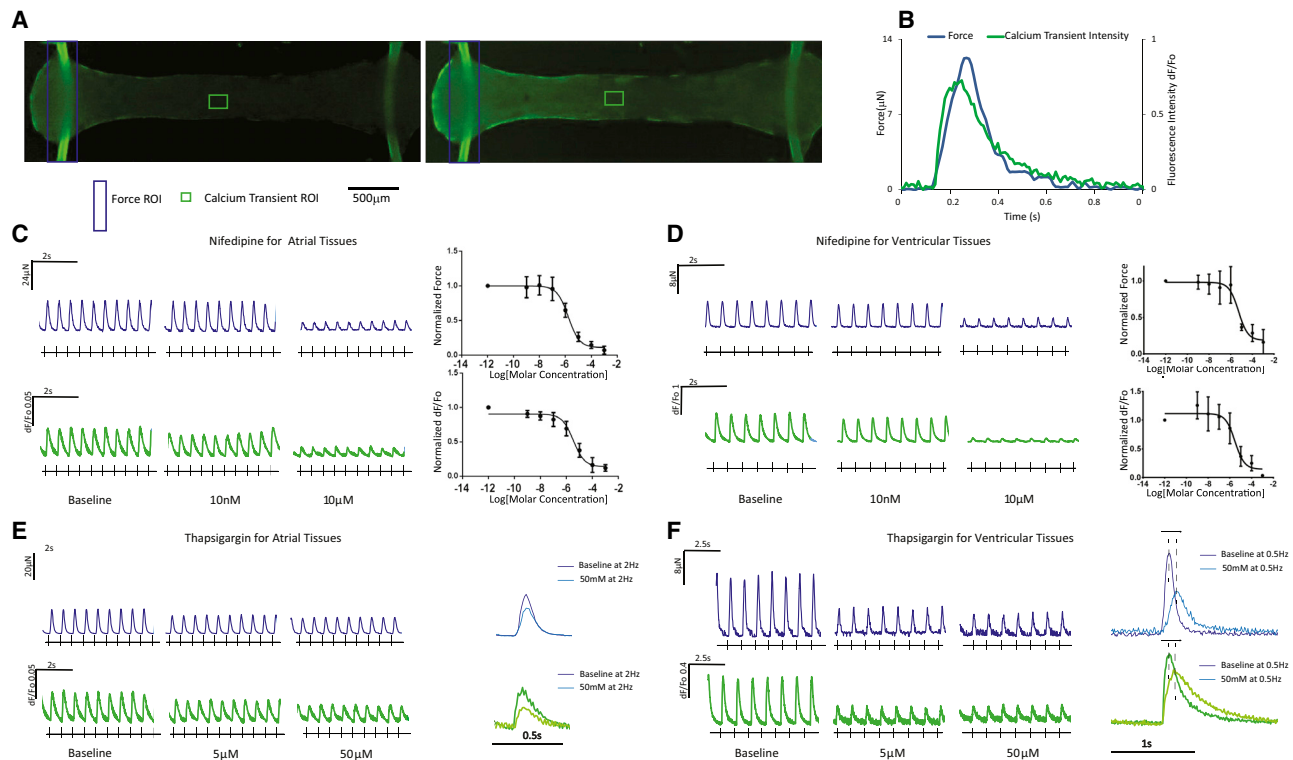


Figure 5. Simultaneous Force and Ca^{2+} Transient Measurements and Their Responses to Drugs in Atrial and Ventricular Tissues

(A) Typical images of biowires loaded with a Ca^{2+} dye (Fluo-4) before (left) and after (right) field stimulation. (B–F) (B) Representative transients. Typical force (blue) and Ca^{2+} transients (green) in (C) atrial or (D) ventricular tissues following the treatment with Nifedipine and the associated dose response (avg \pm stdev, $n = 3$) or treatment with Thapsigargin in (E) atrial or (F) ventricular tissues along with overlays of forces and Ca^{2+} transients before (baseline) and after Thapsigargin addition. Atrial tissues were derived from HES3 hESC-CM and ventricular from BJ1D iPSC-CM. See also Videos S5 and S6.

from patients enrolled in the NHLBI HyperGEN study, one of the largest epidemiological studies focusing on left ventricular hypertrophy (LVH) in families with primary hypertension, which started recruiting in 1996 (Williams et al., 2000). We compared ventricular tissues generated from iPSC-CMs obtained from hypertensive participants with clear evidence of left ventricular hypertrophy (affected group) versus participants without ventricular hypertrophy (non-affected group) (Figure 6A).

Although the underlying basis for the phenotypic differences between the affected group and non-affected group is unknown, hypertension and the associated cardiac responses to the increased workloads generally represent a polygenic disorder. Thus, we hypothesized that chronic electrical conditioning protocols, designed to mimic the chronic increases in cardiac workloads arising from hypertension, will uncover differences between the patient groups. Accordingly, tissues were conditioned during the first 6 weeks using our standard ventricular

conditioning protocols. Thereafter, electrical stimulation was continued at 6 Hz for 1 additional week, after which the stimulation frequency was reduced to 3 Hz and maintained for up to 6 months (Figure 6B). Total cultivation times were up to 8 months.

In contrast to previous studies focusing on monogenic cardiac diseases, modeling of polygenic disease necessitates more comprehensive genetic profiling analysis. Interestingly, profiling of RNA expression in conditioned ventricular biowires (Figure 6C) after 8 months of culture demonstrates distinct gene expression profiles for affected versus non-affected patients as revealed from gene set enrichment analyses. These studies were performed in two separate batches of biowires generated from affected and non-affected participants as summarized in Figure 6C. In both batches, enrichment in 25 cardiac toxicity and canonical signaling pathways was consistently uncovered in biowires from affected versus non-affected patients (Figure 6D),

(E) Conduction velocity maps for atrial and ventricular tissues. Scale bars, 500 μm for atrial and 200 μm for ventricular tissue.

(F) Summary of propagation velocity. (Avg \pm stdev, $n \geq 4$; Mann-Whitney test).

(G–M) Chamber-specific AP profiles of (G) atrial and (H) ventricular tissues. Summary data of: (I) AP amplitudes, (J) maximum diastolic potentials (MDP), (K) upstroke velocities, (L) AP duration measure at 30%, (APD₃₀), 50% (APD₅₀) and 90% (APD₉₀) repolarization, (M) APD₃₀/APD₉₀ ratios (APD30/90) (Avg \pm stdev, $n \geq 3$; one-way ANOVA or ANOVA on ranks).

Atrial tissues were created from HES3 hESC-CM and ventricular from BJ1D iPSC-CM. See also Figures S3, S4, S5, S6, and S7 and Video S3 and S4.

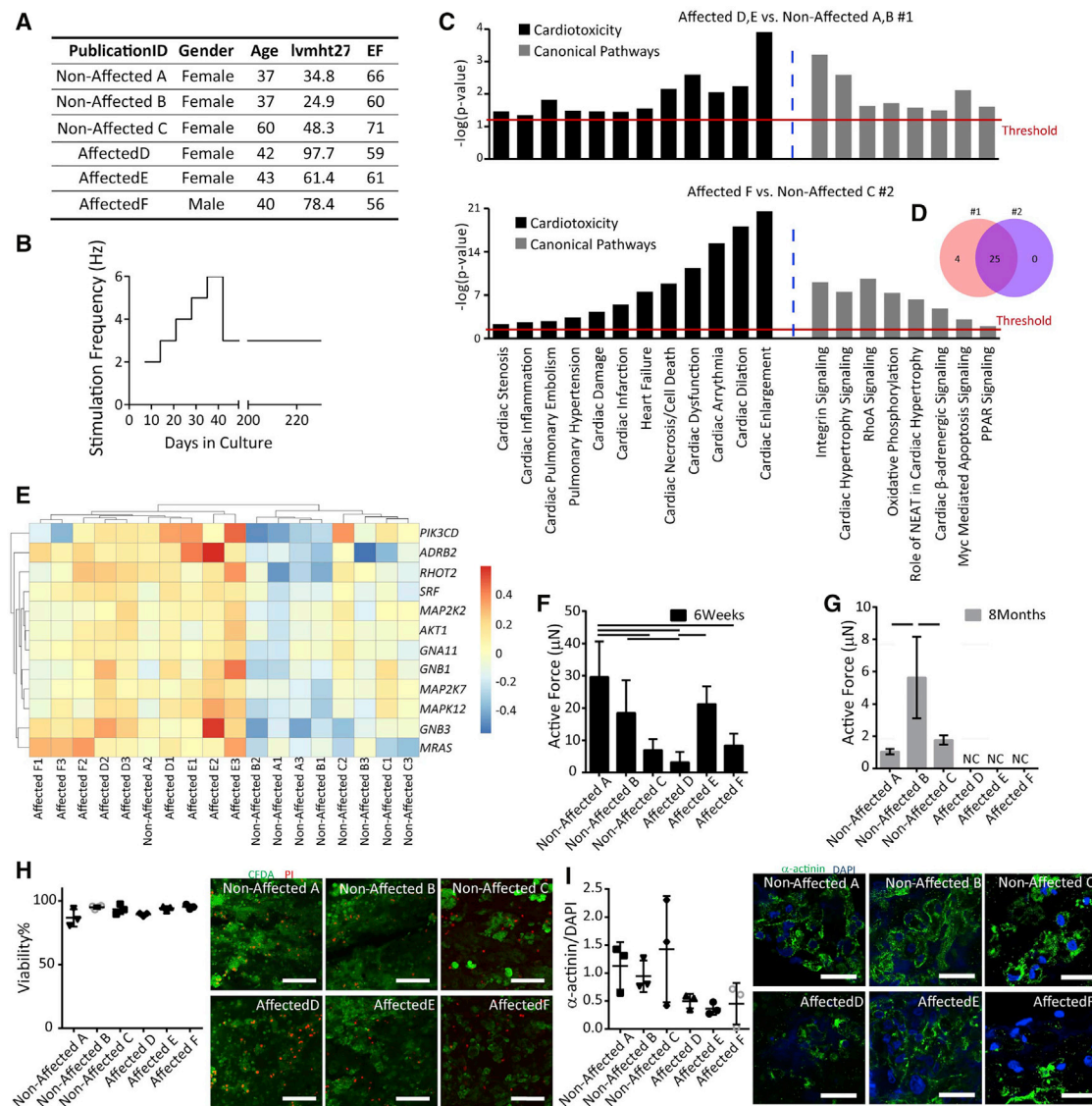


Figure 6. Biowire II Platform Enables Cardiac Disease Modeling

(A) Summary of clinical features, hypertrophy index (lvmt27) and ejection fraction (EF), of hypertensive patients contributing iPSCs.

(B) Long-term electrical conditioning protocol mimicking chronic increased workloads in ventricular tissues created from patient iPSC-CMs.

(C) Gene Set Enrichment Analysis (GSEAs) was performed in two independent experiments (non-affected A, B versus affected D, E; non-affected C versus affected F) revealing enrichment in the affected groups for genes associated with cardiotoxicity and cardiac related canonical pathways (determined by IPA Tox List analysis).

(D) Venn diagram indicates overlap of enriched signaling pathways related to cardiotoxicity from the two experiments. The functional categories shown are ones with Benjamini-Hochberg multiple correction $p \leq 0.05$.

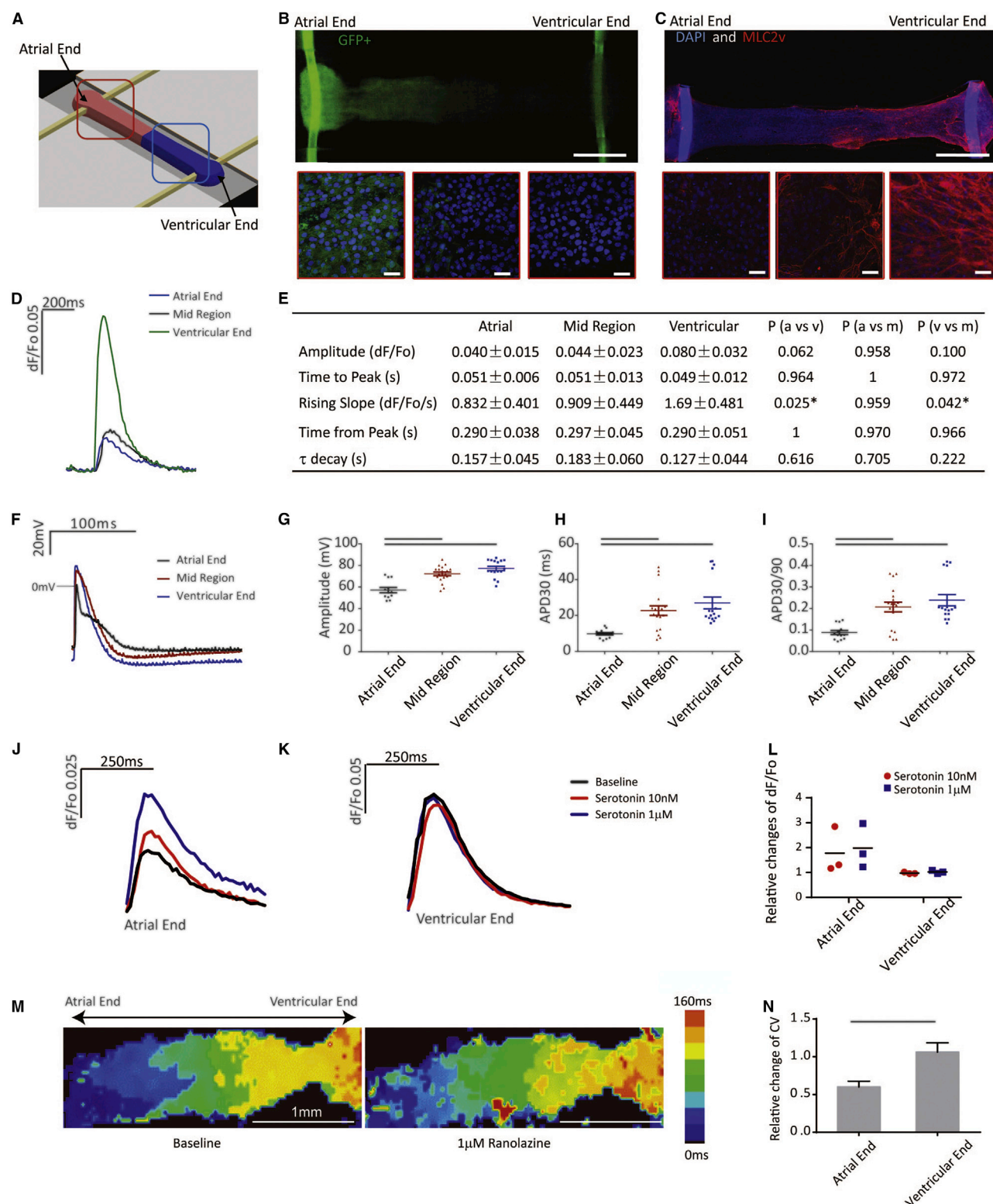
(E) Heatmap showing a sub-set of genes related to cardiac hypertrophy.

(F) Active force was reduced in tissues derived from the patients exhibiting left ventricular hypertrophy in response to a prolonged hypertension (affected D versus affected E, $p = 0.0387$) compared to the non-affected groups (non-affected A versus affected D, $p = 0.0006$; non-affected A versus affected F, $p = 0.0023$; non-affected B versus affected D, $p = 0.0382$, One way ANOVA with Tukey's test) after 6 weeks in culture.

(G) Active force was absent in all tissues from the affected (affected D, E and F) versus non-affected participants (non-affected A, B, and C) after 8 months culture period.

(H) Live (green) and dead (red) staining of tissues at the end of 8 month culture period. Viability was quantified with no significant differences among the groups (avg \pm stdev, $n=3$, ANOVA on ranks). Scale bar, 100 μ m.

(I) Confocal images and quantification of the presence of sarcomeric α -actinin (green) counterstained with DAPI (Blue), Scale bar, 30 μ m (one-way ANOVA with Tukey's test).



(legend on next page)

including pathways broadly linked to pathological remodeling in cardiovascular disease such as cardiac enlargement, cardiac dilatation, cardiac dysfunction, heart failure, and cardiac hypertrophy signaling (Figure 6C). Analysis of the genes related to cardiac hypertrophy and heart failure within individual replicates of independent experimental groups further indicates clear upregulation in all samples derived from the affected participants (Figure 6E), with only one of 3 replicates from one of the non-affected participants (non-affected A) exhibiting a relatively high expression of the hypertrophy associated genes (Figure 6E).

Consistent with these differences in mRNA expression, long-term culturing for 8 months lead to profound differences in contractile function between biowires from the affected participants compared to the non-affected, with all 3 affected samples generating virtually no force compared to the non-affected samples (Figures 6F and 6G). Despite these profound differences in contractile function, no differences in cell viability (Figure 6H) or cardiomyocyte content (Figure 6I) were observed in the biowires from the two groups of participants.

Engineering of Atrioventricular Biowires

A potential advantage of our biowire platform is the ability to generate composite cardiac tissues containing atrial and ventricular zones, which would allow efficient screening of differential responses to agents with chamber-specific actions. With this in mind, we spatially patterned heteropolar biowires by adding atrial and ventricular CMs to opposite ends of the microwells (Figure 7A) as validated using GFP fluorescence to identify atrial CMs (Figure 7B, Video S7) and MLC2v staining to identify ventricular CMs (Figure 7C). As expected, the transition zone between the atrial and ventricular ends was $\sim 200\ \mu\text{m}$ wide and showed mixed atrial and ventricular properties (Figures 7B and 7C). Functionally, Ca^{2+} transients were larger and rose more rapidly, while APs showed distinct properties at the ventricular end compared to the atrial end, with intermediate properties in the transition zone (Figures 7D–7I).

To illustrate the utility of such preparations, we examined the effects of the 5-HT agonist, serotonin and the rapid voltage-gated Na^+ channel blocker, ranolazine, which are reported to have preferential atrial effects (Burashnikov et al., 2007). Indeed, serotonin increased Ca^{2+} transients in the atrial, not ventricular, ends of biowires (Kaumann et al., 1991) (Figures 7J–7L), while

Ranolazine decreased conduction velocity in atrial regions without affecting ventricular zones, consistent with preferential blockade of Na^+ in atrial CMs (Figures 7M and 7N).

DISCUSSION

Biowire II platform uniquely combines the benefits of organ-on-a-chip engineering and organoid self-assembly to enable noninvasive, multiparametric readouts of physiological responses. These capabilities are made possible by the self-assembly of tissues between two parallel POMaC wires, matching the mechanical properties of the native cardiac tissue (10–500 kPa [Nagueh et al., 2004; Omens, 1998]) and allowing the force to be continuously measured. The configuration enables cultivation of multiple tissues suspended on only 2 parallel wires, in contrast to the microcantilever approach that requires a pair of silicone posts for a cultivation of a single tissue.

Common platforms for cultivation of 3D cardiac microtissues incorporate PDMS because of its biocompatibility and ease of use (Eschenhagen et al., 2012; Lind et al., 2017a; Nunes et al., 2013; Schaaf et al., 2011; Tulloch et al., 2011) but at the expense of absorption of small hydrophobic molecules (Toepke and Beebe, 2006). Although the Biowire II platform is plastic, the small amount of drug absorption is associated with the POMaC wires and the presence of low absorption polyurethane adhesive (Domansky et al., 2013) used to secure the POMaC wires to the plastic. Fortunately, functional Biowire II devices can also be constructed without the adhesive.

A major advantage of the platform is the ability to continuously and non-invasively measure Ca^{2+} transients and active force, in combination with other endpoint measurements such as conduction velocity and APs. Future developments will enable simultaneous force, Ca^{2+} transient and electrical measurements.

Another advantage is a small number of input CMs (i.e., ~ 0.1 million/tissue) compared with many previous studies requiring 0.5–2 million cells/tissue (Mannhardt et al., 2016; Nunes et al., 2013; Ronaldson-Bouchard et al., 2018). Consequently, although the absolute active force per tissue is significantly lower in the current work compared to that reported in other studies (Jackman et al., 2016; Mannhardt et al., 2016; Riegler et al., 2015; Ronaldson-Bouchard et al., 2018), the force per cross-sectional area (or per cell) is on the order of those reported

Figure 7. Engineering of Atrioventricular Tissues

(A) Schematics of the experimental set-up.

(B) Atrial (GFP+) and ventricular (GFP-) CMs are placed at the opposite ends of the biowires suspended between two POMaC wires exhibiting green autofluorescence. Zoomed images from right-to-left are taken from the atrial end, the mid region (mixed atrial and ventricular) and the ventricular end. (Scale bar, 0.5 mm, insets scale bar, 30 μm).

(C) Only ventricular end of the tissues stains positive for myosin light chain 2v (MLC2v). Zoomed-in insets from the atrial end, mid region, and ventricular end were compared. Nuclei are counterstained with DAPI. POMaC polymer wires exhibit blue autofluorescence (Scale bar, 0.5mm, insets scale bar, 30 μm).

(D) Representative traces of Ca^{2+} transients from atrial, mid and ventricular region of atrioventricular tissues.

(E–K) (E) Quantification of Ca^{2+} transients, $\text{avg} \pm \text{stdev}$, $n=5$, one-way ANOVA, *denotes significant difference. AP (F) profiles, (G) amplitude, (H) APD30, and (I) APD30/90 from atrial, mid, and ventricular regions were compared ($\text{avg} \pm \text{SEM}$, $n \geq 3$, one-way ANOVA or ANOVA on ranks). Representative traces of Ca^{2+} transients in response to serotonin at (J) the atrial end and (K) the ventricular end of the tissue.

(L) Change in Ca^{2+} transient amplitude in response to serotonin normalized to the baseline. ($n = 3$, two way ANOVA with Sidak's test).

(M) Optical mapping of impulse propagation before and after application of 1 μM ranolazine.

(N) Quantification of the conduction velocity upon ranolazine application after normalization to the baseline ($\text{avg} \pm \text{stdev}$, $n = 4$, $p = 0.0286$, Mann-Whitney test). In J–N, both ends of the tissue were derived from HES3 hESC.

See also Video S7.

in other studies (Figure S4O). These results suggest a possible community effect, such that the contribution of CM number to the collective contractile force in a tissue is non-linear. Yet, fold increase in the force between 1–3 Hz was much higher in the current ventricular preparations compared to those reported in a recent landmark study (Ronaldson-Bouchard et al., 2018).

Our data indicate that both distinct directed differentiation protocols and the electrical conditioning contribute to atrial versus ventricular phenotype divergence in the platform. Electrical conditioning appeared to be particularly effective for ventricular preparations, causing upregulation of high-density lipoprotein genes consistent with developmental metabolic changes that decrease the reliance of adult cardiomyocytes on glycolysis while also strongly promoting sarcomeric organization, the expression of chamber-specific proteins such as MLC2v and generating quiescent tissues at the end of cultivation in the absence of external stimulation. These tissues display a robust positive FFR, PRP, a fast conduction velocity and for the first time displaying notches in the AP profile. Consistent with the native adult atrial muscle physiology (Iwashiro et al., 1997), the atrial biowires display a relatively flat FFR, minimal PRP and a slower conduction velocity.

By contrast, the minimum diastolic potential of the tissues (−70 mV) was still somewhat depolarized compared to the adult myocardium levels (−80 to −90 mV) (Drouin et al., 1995), especially in atrial biowires, and this correlated with relatively slow upstroke velocities (~110 mV/ms) compared to the adult myocardium (254–303 mV/ms) despite being faster than fetal myocardium (5–13 mV/ms) (Koncz et al., 2011; Mummery et al., 2003).

Chamber-specific cardiotoxicity is considered a major issue (Santini and Ricci, 2001). In this regard, we provide evidence for chamber-specific drug responses. We also observed higher expression levels of KCNJ2 responsible for Kir2.1 protein production and the corresponding I_{K1} current in ventricular tissues compared to atrial tissues.

The Biowire platform may enable us to fully understand the disease mechanisms responsible for progression from LVH to heart failure. Although all the NHLBI HyperGEN-LVH study patients suffer from prolonged hypertension, associated with marked elevations in cardiac workloads, they present with highly variable LVH. Our blinded studies allowed the identification of three cell lines derived from affected hypertensive participants with the greatest amount of LVH versus non-affected participants with normal LV mass and contractile function. Clearly, the tissues derived from the non-affected participants were better at resisting the rapid pacing protocol and maintaining contractility compared to those derived from the affected participants. The identified RNA expression differences between the two groups reflect the underlying disease phenotype of LVH.

To generate atrioventricular biowires from a single cell source, we used HES3-NKX2-5^{eGFP/w} cells; and to facilitate imaging of cell location, we used a combination of GFP+ HES3 atrial CM at one end and BJ1D ventricular cells at the other end. Although BJ1D cells enabled us to prepare ventricular tissues with high conduction velocities (31.8 ± 7.9 cm/s), in the range of adult

myocardium (30–100 cm/s), HES3 ventricular preparations achieved velocities of only 5.5 ± 1.3 cm/s, leading to relatively low conduction velocities of HES3 atrio-ventricular preparations.

The effects of serotonin on the cardiovascular system are complex, consisting of bradycardia or tachycardia, hypotension or hypertension, and vasodilation or vasoconstriction (Saxena and Villalón, 1990). It has been reported to cause positive inotropy in atrial CMs and no inotropic effect in ventricular CMs (Jahnel et al., 1992). Atrioventricular biowires were able to capture the complex effect of serotonin, revealing the positive inotropic effect of serotonin on the atrial end but not the ventricular end. Ranolazine is currently in clinical trials with Gilead. This drug is largely a Na⁺ channel blocker, affecting both atria and ventricle, albeit in different ways. There is some controversy related to how and whether it has atrial-selective effects (Jahnel et al., 1992). Conduction velocity significantly slowed down at the atrial end, but not at the ventricular end, after introduction of ranolazine. The half-inactivation voltage of atrial CMs is more negative than ventricular CMs; therefore, more sodium channels inactivate at baseline membrane for atrial CMs at stroke or takeoff point compared with ventricular CMs. Because ranolazine is effective on the inactive sodium channel, it affects atrial more than ventricular cells (Burashnikov et al., 2007). Thus, heteropolar biowires enable us to capture the effects of drugs with complex or incompletely understood mechanisms of action.

STAR★METHODS

Detailed methods are provided in the online version of this paper and include the following:

- KEY RESOURCES TABLE
- CONTACT FOR REAGENT AND RESOURCE SHARING
- EXPERIMENTAL MODEL AND SUBJECT DETAILS
 - Cell Lines
 - Primary Cultures
- METHOD DETAILS
 - Device Fabrication
 - Hydrogel Preparation
 - Electrical Stimulation Chamber Fabrication
 - Generation of Engineered Cardiac Tissues
 - Electrical Stimulation Protocols
 - Atrial and Ventricular Tissue RNA Sequencing
 - Gene set enrichment analysis
 - Gene Expression for Patient Derived Cells
 - Elastic Modulus of Polymer Wires
 - Polymer Wire Force-Displacement Curves
 - Finite Element Modeling (FEM)
 - Active and Passive Force for Cardiac Tissues
 - Absorption Testing
 - Immunostaining and Confocal Microscopy
 - Transmission Electron Microscopy
 - Contractile and Ca²⁺ Transients
 - Intracellular Recordings
 - Optical Mapping
- QUANTIFICATION AND STATISTICAL ANALYSIS
- DATA AND SOFTWARE AVAILABILITY

SUPPLEMENTAL INFORMATION

Supplemental Information includes seven figures and seven videos and can be found with this article online at <https://doi.org/10.1016/j.cell.2018.11.042>.

ACKNOWLEDGMENTS

This work was funded by the Canadian Institutes of Health Research (CIHR) Operating Grants (MOP-126027, MOP-137107, and MOP-142382), Natural Sciences and Engineering Research Council of Canada (NSERC) Discovery Grant (RGPIN 326982-10), NSERC-CIHR Collaborative Health Research Grant (CHRP 493737-16), and National Institutes of Health Grants 2R01 HL076485, UG3 EB025765, P41 EB002520 (to G.V.N.) and U01 HL107437, R01 HL125580 (to U.B.). P.H.B. holds a Tier 1 Canada Research Chair (CIHR). B.C. holds a Tier 2 Canada Research Chair (CIHR). M.R. was supported by NSERC Steacie Fellowship and Canada Research Chair. Y.Z. was supported by NSERC Post-graduate Fellowship, TOEP NSERC CREATE, and Ted Rogers Center for Heart Research Doctoral Award. The authors would like to acknowledge the help of Stasja Drecun, Steven Liao, Sueng Doo (Charlie) Yang, and Friday Anighoro with data analysis. The authors would also like to acknowledge Michael Dunn, Mark Rekhter, Gary Gintant, Robert Willette, and Khuram Chaudhary for helpful discussions; Iran Rashedi and Armand Keating for a kind gift of MSCs; and Blake Anson of the CDI for the kind gift of MyCells.

AUTHOR CONTRIBUTIONS

Conceptualization, Y.Z., N.R., P.H.B., and M.R.; Methodology, Y.Z., N.R., B.Z., P.H.B., and M.R.; Software development, Y.Z., K.R.-B. and G.C.; Validation, Y.Z., N.R., N.T.F., R.A.-S., E.Y.W., P.A., U.B., P.H.B., A.W., H.N., and M.R.; Formal Analysis, Y.Z., N.T.F., N.R., R.A.-S., E.Y.W., D.J., P.A., B.C., A.W., H.N., and L.D.H.; Investigation, Y.Z., N.T.F., N.R., R.A.-S., E.Y.W., and P.A.; Resources, P.H.B., M.R., U.B., G.M.K., A.P., J.H.L., S.P., and L.D.H.; Data Curation, Y.Z., N.R., A.P., U.B., P.H.B., and M.R.; Writing – Original Draft, Y.Z., N.R., P.H.B., M.R.; Writing – Review & Editing, N.T.F., M.R., P.H.B., B.C., G.V.-N., G.M.K., B.Z., U.B., S.P., J.H.L., N.R., A.W.; Visualization, Y.Z., B.Z., E.Y.W., P.H.B., and M.R.; Supervision, P.H.B. and M.R.; Project Administration, Y.Z., N.R., N.T.F., R.A.-S., P.H.B., and M.R.; Funding Acquisition, P.H.B. and M.R.

DECLARATION OF INTERESTS

Y.Z., B.Z., K.R.B., G.V.-N., and M.R. are co-founders and shareholders of TARA Biosystems Inc; N.T.F. and R.A.-S. are employees and shareholders of the company; M.R. and G.V.N. are also on the Board of Directors and receive compensation for this role. Y.Z., B.Z., and M.R. are inventors of a patent application on Biowire II platform related to this work (Pub.No.: US20160282338A1) which has been licensed to TARA Biosystems Inc. M.R., P.A., and U.B. are inventors of a patent application on cell line specific disease modeling related to this work. M.R. Y.Z. N.R. and P.B. are inventors of a patent application related to atrial and ventricular specification. G.M.K. is a scientific cofounder, advisor, and equity holder of BlueRock Therapeutics. All other authors have no competing interests.

Received: August 14, 2018
Revised: September 19, 2018
Accepted: November 28, 2018
Published: January 24, 2019

REFERENCES

Aggarwal, P., Turner, A., Matter, A., Kattman, S.J., Stoddard, A., Lorier, R., Swanson, B.J., Arnett, D.K., and Broeckel, U. (2014). RNA expression profiling of human iPSC-derived cardiomyocytes in a cardiac hypertrophy model. *PLoS ONE* 9, e108051.
Ahn, S., Ardoña, H.A.M., Lind, J.U., Eweje, F., Kim, S.L., Gonzalez, G.M., Liu, Q., Zimmerman, J.F., Pyrgiotakis, G., Zhang, Z., et al. (2018). Mussel-inspired

3D fiber scaffolds for heart-on-a-chip toxicity studies of engineered nanomaterials. *Anal. Bioanal. Chem.* <https://doi.org/10.1007/s00216-018-1106-7>.

Asp, J., Synnnergren, J., Jonsson, M., Dellgren, G., and Jeppsson, A. (2012). Comparison of human cardiac gene expression profiles in paired samples of right atrium and left ventricle collected in vivo. *Phys. Genom.* 44, 89–98.

Blatter, L.A. (2017). The intricacies of atrial calcium cycling during excitation-contraction coupling. *J. Gen. Physiol.* 149, 857–865.

Bray, N.L., Pimentel, H., Melsted, P., and Pachter, L. (2016). Near-optimal probabilistic RNA-seq quantification. *Nat. Biotechnol.* 34, 525–527.

Burashnikov, A., and Antzelevitch, C. (2008). How Do Atrial-Selective Drugs Differ From Antiarrhythmic Drugs Currently Used in the Treatment of Atrial Fibrillation? *J. Atr. Fibrillation* 1, 98–107.

Burashnikov, A., Di Diego, J.M., Zygmunt, A.C., Belardinelli, L., and Antzelevitch, C. (2007). Atrium-selective sodium channel block as a strategy for suppression of atrial fibrillation: differences in sodium channel inactivation between atria and ventricles and the role of ranolazine. *Circulation* 116, 1449–1457.

Castle, N.A., and Slawsky, M.T. (1993). Characterization of 4-aminopyridine block of the transient outward K⁺ current in adult rat ventricular myocytes. *J. Pharmacol. Exp. Ther.* 265, 1450–1459.

Chen, L.Y., Sotoodehnia, N., Bůžková, P., Lopez, F.L., Yee, L.M., Heckbert, S.R., Prineas, R., Soliman, E.Z., Adabag, S., Konety, S., et al. (2013). Atrial fibrillation and the risk of sudden cardiac death: the atherosclerosis risk in communities study and cardiovascular health study. *JAMA Intern. Med.* 173, 29–35.

Cyganek, L., Tiburcy, M., Sekeres, K., Gerstenberg, K., Bohnenberger, H., Lenz, C., Henze, S., Stauske, M., Salinas, G., Zimmermann, W.H., et al. (2018). Deep phenotyping of human induced pluripotent stem cell-derived atrial and ventricular cardiomyocytes. *JCI Insight* 3. <https://doi.org/10.1172/jci.insight.99941>.

Davia, K., Davies, C.H., and Harding, S.E. (1997). Effects of inhibition of sarcolemmal reticulum calcium uptake on contraction in myocytes isolated from failing human ventricle. *Cardiovasc. Res.* 33, 88–97.

Dawodu, A.A., Monti, F., Iwashiro, K., Schiari, M., Chiavarelli, R., and Puddu, P.E. (1996). The shape of human atrial action potential accounts for different frequency-related changes in vitro. *Int. J. Cardiol.* 54, 237–249.

Domansky, K., Leslie, D.C., McKinney, J., Fraser, J.P., Sliz, J.D., Hamkins-Indik, T., Hamilton, G.A., Bahinski, A., and Ingber, D.E. (2013). Clear castable polyurethane elastomer for fabrication of microfluidic devices. *Lab Chip* 13, 3956–3964.

Drouin, E., Charpentier, F., Gauthier, C., Laurent, K., and Le Marec, H. (1995). Electrophysiologic characteristics of cells spanning the left ventricular wall of human heart: evidence for presence of M cells. *J. Am. Coll. Cardiol.* 26, 185–192.

Eisen, A., Ruff, C.T., Braunwald, E., Nordio, F., Corbalán, R., Dalby, A., Dorobantu, M., Mercuri, M., Lanz, H., Rutman, H., et al. (2016). Sudden Cardiac Death in Patients With Atrial Fibrillation: Insights From the ENGAGE AF-TIMI 48 Trial. *J. Am. Heart Assoc.* 5. <https://doi.org/10.1161/JAHA.116.003735>.

Eschenhagen, T., Eder, A., Vollert, I., and Hansen, A. (2012). Physiological aspects of cardiac tissue engineering. *Am. J. Physiol. Heart Circ. Physiol.* 303, H133–H143.

Gaborit, N., Le Bouter, S., Szuts, V., Varro, A., Escande, D., Nattel, S., and Demolombe, S. (2007). Regional and tissue specific transcript signatures of ion channel genes in the non-diseased human heart. *The Journal of physiology* 582, 675–693.

Grandi, E., Pandit, S.V., Voigt, N., Workman, A.J., Dobrev, D., Jalife, J., and Bers, D.M. (2011). Human atrial action potential and Ca²⁺ model: sinus rhythm and chronic atrial fibrillation. *Circ. Res.* 109, 1055–1066.

Hinson, J.T., Chopra, A., Nafissi, N., Polacheck, W.J., Benson, C.C., Swist, S., Gorham, J., Yang, L., Schafer, S., Sheng, C.C., et al. (2015). HEART DISEASE. Titin mutations in iPS cells define sarcomere insufficiency as a cause of dilated cardiomyopathy. *Science* 349, 982–986.

- Huebsch, N., Loskill, P., Deveshwar, N., Spencer, C.I., Judge, L.M., Mandegar, M.A., Fox, C.B., Mohamed, T.M., Ma, Z., Mathur, A., et al. (2016). Miniaturized iPS-Cell-Derived Cardiac Muscles for Physiologically Relevant Drug Response Analyses. *Sci. Rep.* 6, 24726.
- Iwashiro, K., Criniti, A., Sinatra, R., Dawodu, A.A., d'Amati, G., Monti, F., Panarale, L., Bernucci, P., Brancaccio, G.L., Vetuschi, A., et al. (1997). Felodipine protects human atrial muscle from hypoxia-reoxygenation dysfunction: a force-frequency relationship study in an in vitro model of stunning. *Int. J. Cardiol.* 62, 107–132.
- Jackman, C.P., Carlson, A.L., and Bursac, N. (2016). Dynamic culture yields engineered myocardium with near-adult functional output. *Biomaterials* 111, 66–79.
- Jahnel, U., Rupp, J., Ertl, R., and Nawrath, H. (1992). Positive inotropic response to 5-HT in human atrial but not in ventricular heart muscle. *Naunyn Schmiedeberg Arch. Pharmacol.* 346, 482–485.
- Kaumann, A.J., Sanders, L., Brown, A.M., Murray, K.J., and Brown, M.J. (1991). A 5-HT₄-like receptor in human right atrium. *Naunyn Schmiedeberg Arch. Pharmacol.* 344, 150–159.
- Koncz, I., Szél, T., Bitay, M., Cerbai, E., Jaeger, K., Fülöp, F., Jost, N., Virág, L., Orvos, P., Tólosi, L., et al. (2011). Electrophysiological effects of ivabradine in dog and human cardiac preparations: potential antiarrhythmic actions. *Eur. J. Pharmacol.* 668, 419–426.
- Lee, J.H., Protze, S.I., Laksman, Z., Backx, P.H., and Keller, G.M. (2017). Human Pluripotent Stem Cell-Derived Atrial and Ventricular Cardiomyocytes Develop from Distinct Mesoderm Populations. *Cell Stem Cell* 21, 179–194.
- Lemoine, M.D., Mannhardt, I., Breckwoldt, K., Prondzynski, M., Flenner, F., Ulmer, B., Hirt, M.N., Neuber, C., Horváth, A., Kloth, B., et al. (2017). Human iPSC-derived cardiomyocytes cultured in 3D engineered heart tissue show physiological upstroke velocity and sodium current density. *Sci. Rep.* 7, 5464.
- Lemoine, M.D., Krause, T., Koivumäki, J.T., Prondzynski, M., Schulze, M.L., Girdauskas, E., Willems, S., Hansen, A., Eschenhagen, T., and Christ, T. (2018). Human Induced Pluripotent Stem Cell-Derived Engineered Heart Tissue as a Sensitive Test System for QT Prolongation and Arrhythmic Triggers. *Circ Arrhythm Electrophysiol* 11, e006035.
- Li, G.R., Feng, J., Wang, Z., Fermini, B., and Nattel, S. (1995). Comparative mechanisms of 4-aminopyridine-resistant I_{to} in human and rabbit atrial myocytes. *Am. J. Physiol.* 269, H463–H472.
- Lian, X., Hsiao, C., Wilson, G., Zhu, K., Hazeltine, L.B., Azarin, S.M., Raval, K.K., Zhang, J., Kamp, T.J., and Palecek, S.P. (2012). Robust cardiomyocyte differentiation from human pluripotent stem cells via temporal modulation of canonical Wnt signaling. *Proc. Natl. Acad. Sci. USA* 109, E1848–E1857.
- Lind, J.U., Busbee, T.A., Valentine, A.D., Pasqualini, F.S., Yuan, H., Yadid, M., Park, S.J., Kotikian, A., Nesmith, A.P., Campbell, P.H., et al. (2017a). Instrumented cardiac microphysiological devices via multimaterial three-dimensional printing. *Nat. Mater.* 16, 303–308.
- Lind, J.U., Yadid, M., Perkins, I., O'Connor, B.B., Eweje, F., Chantre, C.O., Hemphill, M.A., Yuan, H., Campbell, P.H., Vlassak, J.J., and Parker, K.K. (2017b). Cardiac microphysiological devices with flexible thin-film sensors for higher-throughput drug screening. *Lab Chip* 17, 3692–3703.
- MacQueen, L.A., Sheehy, S.P., Chantre, C.O., Zimmerman, J.F., Pasqualini, F.S., Liu, X., Goss, J.A., Campbell, P.H., Gonzalez, G.M., Park, S.-J., et al. (2018). A tissue-engineered scale model of the heart ventricle (Nature Biomedical Engineering).
- Mannhardt, I., Breckwoldt, K., Letuffe-Brenière, D., Schaaf, S., Schulz, H., Neuber, C., Benzin, A., Werner, T., Eder, A., Schulze, T., et al. (2016). Human Engineered Heart Tissue: Analysis of Contractile Force. *Stem Cell Reports* 7, 29–42.
- Mathur, A., Loskill, P., Shao, K., Huebsch, N., Hong, S., Marcus, S.G., Marks, N., Mandegar, M., Conklin, B.R., Lee, L.P., and Healy, K.E. (2015). Human iPSC-based cardiac microphysiological system for drug screening applications. *Sci. Rep.* 5, 8883.
- Mummery, C., Ward-van Oostwaard, D., Doevendans, P., Spijker, R., van den Brink, S., Hassink, R., van der Heyden, M., Opthof, T., Pera, M., de la Riviere, A.B., et al. (2003). Differentiation of human embryonic stem cells to cardiomyocytes: role of coculture with visceral endoderm-like cells. *Circulation* 107, 2733–2740.
- Nagueh, S.F., Shah, G., Wu, Y., Torre-Amione, G., King, N.M., Lahmers, S., Witt, C.C., Becker, K., Labeit, S., and Granzier, H.L. (2004). Altered titin expression, myocardial stiffness, and left ventricular function in patients with dilated cardiomyopathy. *Circulation* 110, 155–162.
- Nunes, S.S., Miklas, J.W., Liu, J., Aschar-Sobbi, R., Xiao, Y., Zhang, B., Jiang, J., Massé, S., Gagliardi, M., Hsieh, A., et al. (2013). Biowire: a platform for maturation of human pluripotent stem cell-derived cardiomyocytes. *Nat. Methods* 10, 781–787.
- O'Hara, T., Virág, L., Varró, A., and Rudy, Y. (2011). Simulation of the undiseased human cardiac ventricular action potential: model formulation and experimental validation. *PLoS Comput. Biol.* 7, e1002061.
- Omens, J.H. (1998). Stress and strain as regulators of myocardial growth. *Prog. Biophys. Mol. Biol.* 69, 559–572.
- Oudit, G.Y., Kassiri, Z., Sah, R., Ramirez, R.J., Zobel, C., and Backx, P.H. (2001). The molecular physiology of the cardiac transient outward potassium current (I_{to}) in normal and diseased myocardium. *J. Mol. Cell. Cardiol.* 33, 851–872.
- Park, I.H., Zhao, R., West, J.A., Yabuuchi, A., Huo, H., Ince, T.A., Lerou, P.H., Lensch, M.W., and Daley, G.Q. (2008). Reprogramming of human somatic cells to pluripotency with defined factors. *Nature* 451, 141–146.
- Pimentel, H., Bray, N.L., Puente, S., Melsted, P., and Pachter, L. (2017). Differential analysis of RNA-seq incorporating quantification uncertainty. *Nat. Methods* 14, 687–690.
- Riegler, J., Tiburcy, M., Ebert, A., Tzatzalos, E., Raaz, U., Abilez, O.J., Shen, Q., Kooreman, N.G., Neofytou, E., Chen, V.C., et al. (2015). Human Engineered Heart Muscles Engraft and Survive Long Term in a Rodent Myocardial Infarction Model. *Circ. Res.* 117, 720–730.
- Ronaldson-Bouchard, K., Ma, S.P., Yeager, K., Chen, T., Song, L., Sirabella, D., Morikawa, K., Teles, D., Yazawa, M., and Vunjak-Novakovic, G. (2018). Advanced maturation of human cardiac tissue grown from pluripotent stem cells. *Nature* 556, 239–243.
- Santini, M., and Ricci, R. (2001). Atrial fibrillation coexisting with ventricular tachycardia: a challenge for dual chamber defibrillators. *Heart* 86, 253–254.
- Saxena, P.R., and Villalón, C.M. (1990). Cardiovascular effects of serotonin agonists and antagonists. *J. Cardiovasc. Pharmacol.* 15 (Suppl 7), S17–S34.
- Schaaf, S., Shibamiya, A., Mewe, M., Eder, A., Stöhr, A., Hirt, M.N., Rau, T., Zimmermann, W.H., Conradi, L., Eschenhagen, T., and Hansen, A. (2011). Human engineered heart tissue as a versatile tool in basic research and preclinical toxicology. *PLoS ONE* 6, e26397.
- Sidorov, V.Y., Samson, P.C., Sidorova, T.N., Davidson, J.M., Lim, C.C., and Wikswo, J.P. (2017). I-Wire Heart-on-a-Chip I: Three-dimensional cardiac tissue constructs for physiology and pharmacology. *Acta Biomater.* 48, 68–78.
- Tiburcy, M., Hudson, J.E., Balfanz, P., Schlick, S., Meyer, T., Chang Liao, M.L., Levent, E., Raad, F., Zeidler, S., Wingender, E., et al. (2017). Defined Engineered Human Myocardium With Advanced Maturation for Applications in Heart Failure Modeling and Repair. *Circulation* 135, 1832–1847.
- Toepke, M.W., and Beebe, D.J. (2006). PDMS absorption of small molecules and consequences in microfluidic applications. *Lab Chip* 6, 1484–1486.
- Tulloch, N.L., Muskheili, V., Razumova, M.V., Korte, F.S., Regnier, M., Hauch, K.D., Pabon, L., Reinecke, H., and Murray, C.E. (2011). Growth of engineered human myocardium with mechanical loading and vascular coculture. *Circ. Res.* 109, 47–59.
- van der Hooft, C.S., Heeringa, J., van Herpen, G., Kors, J.A., Kingma, J.H., and Stricker, B.H. (2004). Drug-induced atrial fibrillation. *J. Am. Coll. Cardiol.* 44, 2117–2124.
- Vicente, J., Johannesen, L., Mason, J.W., Crumb, W.J., Pueyo, E., Stockbridge, N., and Strauss, D.G. (2015). Comprehensive T wave morphology assessment in a randomized clinical study of dofetilide, quinidine, ranolazine,

- and verapamil. *J. Am. Heart Assoc.* **4**. <https://doi.org/10.1161/JAHA.114.001615>.
- Wang, G., McCain, M.L., Yang, L., He, A., Pasqualini, F.S., Agarwal, A., Yuan, H., Jiang, D., Zhang, D., Zangi, L., et al. (2014). Modeling the mitochondrial cardiomyopathy of Barth syndrome with induced pluripotent stem cell and heart-on-chip technologies. *Nat. Med.* **20**, 616–623.
- Williams, R.R., Rao, D.C., Ellison, R.C., Arnett, D.K., Heiss, G., Oberman, A., Eckfeldt, J.H., Leppert, M.F., Province, M.A., Mockrin, S.C., and Hunt, S.C. (2000). NHLBI family blood pressure program: methodology and recruitment in the HyperGEN network. Hypertension genetic epidemiology network. *Ann. Epidemiol.* **10**, 389–400.
- Yang, L., Soonpaa, M.H., Adler, E.D., Roepke, T.K., Kattman, S.J., Kennedy, M., Henckaerts, E., Bonham, K., Abbott, G.W., Linden, R.M., et al. (2008). Human cardiovascular progenitor cells develop from a KDR+ embryonic-stem-cell-derived population. *Nature* **453**, 524–528.
- Zang, W.J., Chen, L.N., Yu, X.J., Fang, P., Lu, J., and Sun, Q. (2005). Comparison of effects of acetylcholine on electromechanical characteristics in guinea-pig atrium and ventricle. *Exp. Physiol.* **90**, 123–130.
- Zhang, B., Montgomery, M., Chamberlain, M.D., Ogawa, S., Korolj, A., Pahnke, A., Wells, L.A., Massé, S., Kim, J., Reis, L., et al. (2016). Biodegradable scaffold with built-in vasculature for organ-on-a-chip engineering and direct surgical anastomosis. *Nat. Mater.* **15**, 669–678.

STAR★METHODS

KEY RESOURCES TABLE

Reagents and Resources	SOURCE	IDENTIFIER
Antibodies		
Mouse monoclonal anti-Troponin T Cardiac Isoform Ab-1 (Clone 13-11)	Thermo Fisher Scientific	Cat#MS295-P; RRID: AB_61808
Rabbit polyclonal anti-Connexin 43 / GJA1	Abcam	Cat#ab11370; RRID: AB_297976
Mouse monoclonal anti-Sarcomeric Alpha Actinin	Abcam	Cat#ab9465; RRID: AB_307264
Rabbit polyclonal anti- MYL9/MYL12A/B (FL-172)	Santa Cruz	Cat# sc-15370; RRID: AB_2148039
Donkey anti-mouse IgG H&L (Alexa Fluor 488)	Abcam	Cat#ab150105
Donkey anti-rabbit IgG H&L (Alexa Fluor 594)	Abcam	Cat#ab150080; RRID: AB_2650602
Alexa Fluor 660 Phalloidin	Invitrogen	Cat#A22285
Goat polyclonal anti-caveolin-3 (N-18)	Santa Cruz	Cat#SC7665; RRID:AB_637945
Mouse monoclonal anti-Vimentin–Cy3	Sigma-Aldrich	Cat#C9080
Donkey anti-goat IgG (Alexa Fluor 647)	Life Technologies	Cat#A21447; RRID:AB_141844
Chemicals, Peptides, and Recombinant Proteins		
Diltiazem HCL	Sigma-Aldrich	Cat#D2521
Dofetilide	Sigma-Aldrich	Cat# PZ0016
Verapamil hydrochloride	Invitrogen	Cat#D1199
(S)-(-)-Blebbistatin	Toronto Research Chemicals	Cat#B592500
Lidocaine	Sigma-Aldrich	Cat# L7757
Milrinone	Sigma-Aldrich	Cat# M4659
E4031	Sigma-Aldrich	Cat# M5060
Nifedipine	Sigma-Aldrich	Cat# N7634
Thapsigargin	Sigma-Aldrich	Cat# T9033
5-HT (Serotonin hydrochloride)	Sigma-Aldrich	Cat# H9523
Ranolazine dihydrochloride	Sigma-Aldrich	Cat# R6152
1,6 dioxane,	Sigma-Aldrich	Cat# 360481
carbon rods	Ladd Research Industries	Cat# 30250
SU-8 2025	MicroChem	Cat#Y11106905001GL
SU-8 2010	MicroChem	Cat#Y1110580500L1GL
Rhodamine B	Sigma-Aldrich	Cat# 83689
Rhodamine 6G	Sigma-Aldrich	Cat# 83697
Polyurethane casting and potting system	GS polymers	GSP1552-2
Critical Commercial Assays		
Fluo-4 NW Calcium Assay Kit	Life Technologies	Cat# F36206
Di-4-ANEPPS	Invitrogen	Cat#90134-00-2
Kreb's Solution	Sigma	K4002
PicoPure RNA Isolation Kit	Thermo Fisher Scientific	KIT0204
RNase-Free DNase Set	QIAGEN	79254
FGM-3 Cardiac Fibroblast Growth Medium-3 BulletKit	Lonza	CC-4526
Software and Algorithms		
Spot Tracker and Enhanced filters	Biomedical Imaging Group	http://bigwww.epfl.ch/sage/soft/spottracker/
MATLAB custom code	This paper	

(Continued on next page)

Continued

Reagents and Resources	SOURCE	IDENTIFIER
pCLAMP	Molecular Devices	https://www.moleculardevices.com/systems/conventional-patch-clamp/pclamp-10-software
Image Pro plus 6	Media cybernetics	http://www.mediacy.com/imageproplus
Deposited data		
RNA sequencing data (Atrial/Ventricular Tissues)	NCBI:GSE114976	The accession number is GSE114976. The release date is May 1 2019.
RNA sequencing data (Disease models)	NCBI:GSE122661	The accession number is GSE122661. The release date is Dec 13 2018.
Other		
Type I Rat Tail Collagen	Corning	Cat#354249
Medium 199	Sigma-Aldrich	Cat#M4530
Aprotinin from bovine lung	Sigma-Aldrich	Cat#A3428
StemPro™-34 SFM	Life Technologies	Cat#10639011
RPMI with L-Glutamine	Life Technologies	Cat#11875-093
B27 plus insulin	Life Technologies	Cat#17504-044
B27 supplement minus insulin 50X	Life Technologies	Cat#A1895601
mTesr	Cedarlane	Cat#05850
IWP4	Miltenyi Biotec, Stemgent	Cat# 04-0036
CHIR 99021	Miltenyi Biotec, Stemgent	Cat# 04-0004
NaOH	Caledon	Cat#7860-1-70
Na HCO ₃	E COM	Cat#SX0320-1
Growth factor reduced matrigel	Corning	Cat#354230
Collagenase type 2	Worthington	Cat#4176
All trans RA	Sigma-Aldrich	Cat#2625
Retinol	Sigma-Aldrich	Cat#7632
DMEM	Thermo Fisher	Cat#11054-080
fetal bovine serum (FBS)	Life Technologies	Cat#12483020
Penicillin-Streptomycin	Thermo Fisher	Cat.#15070063
Non-glare polystyrene sheet	Plaskolite, Inc	https://www.plaskolite.com
Trypsin/EDTA 0.05%	Life Technologies	Cat.#25300054
Cells		
HES2	Wicell	Cat.# ES02; RRID: CVCL_D093
HES3-NKX2-5 ^{gfp/w}	Gift from Drs. E. Stanley and A. Elefanty, Monash University, AU	N/A
MSC-iPSC1 line	Gift from Dr. G. Daley, Harvard Medical School, US (Park et al., 2008)	N/A
BJ1D cell line	Gift from Dr. William Stanford, now at Ottawa Heart Institute	N/A
iCell	FUJIFILM Cellular Dynamics Inc.	R1007
iCell ²	Cellular dynamicsFUJIFILM Cellular Dynamics Inc.	R1007
C2A hiPSC	Material Transfer Agreements between GVN lab and Stephen Duncan, University of Wisconsin	N/A
Non-affected A	FUJIFILM Cellular Dynamics Inc.	01078.716.CM001
Non-affected B	FUJIFILM Cellular Dynamics Inc.	01082.726.CM001
Non-affected C	FUJIFILM Cellular Dynamics Inc.	01320.716.CM001

(Continued on next page)

Continued

Reagents and Resources	SOURCE	IDENTIFIER
Affected D	FUJIFILM Cellular Dynamics Inc.	01125.716.CM001
Affected E	FUJIFILM Cellular Dynamics Inc.	01135.700.CM001
Affected F	FUJIFILM Cellular Dynamics Inc.	01187.704.CM001
NHCF	Lonza	CC-2904
SPRD Sprague-Dawley Rattus norvegicus	Charles River	RRID: 1566457

CONTACT FOR REAGENT AND RESOURCE SHARING

Further information and requests for reagents may be directed to, and will be fulfilled by, the Lead Contact, Milica Radisic (m.radisic@utoronto.ca).

EXPERIMENTAL MODEL AND SUBJECT DETAILS

Cell Lines

Predominantly ventricular cardiomyocytes (CMs) were derived from the human embryonic stem cell (hESC) lines HES2 (Female) and HES3-NKX2-5^{eGFP/w} (Female) using the embryoid body (EB) (Yang et al., 2008) differentiation protocol and the human induced pluripotent stem cell (hiPSC) line BJ1D (male) (Nunes et al., 2013) using the monolayer differentiation protocols (Lian et al., 2012) as previously described. Ventricular cell populations contained $74.7 \pm 6.3\%$ ($n = 9$) of CMs on average, based on cardiac troponin T expression analysis using flow cytometry, at the end of directed differentiation protocols.

C2A hiPSC derived cardiomyocytes were differentiated in EBs as previously described (Ronaldson-Bouchard et al., 2018). Gender information cannot be provided according to the terms used to obtain the line.

iCell and iCell² cardiomyocytes were purchased from Cellular Dynamics International (CDI) Inc, Madison, Wisconsin and used according to the manufacturer's instructions. Gender information should be available from the company upon request.

Induced pluripotent stem cells were derived from the non-affected A (Female), non-affected B (Female), non-affected C (Female), affected D (Female), affected E (Female), and affected F (Male) patients and differentiated into CMs by CDI. CDI kindly provided these differentiated CMs for the project.

Predominantly atrial CMs were derived from HES3-NKX2-5^{eGFP/w} hESCs and MSC-iPSC1 (Park et al., 2008) using an atrial-specific EB differentiation protocol as described (Lee et al., 2017). Briefly, all trans retinoic acid (0.5 μ M, Sigma) was added during the cardiac mesoderm specification stage (days 3-5 of differentiation) to promote atrial cardiogenesis. At day 20 of differentiation, atrial CMs from HES3-NKX2-5^{eGFP/w} hESCs were analyzed and defined based on the proportion of NKX2.5+, cTNT+ and MLC2v- cells using flow cytometry, $79.1 \pm 8.0\%$, $n = 10$. For predominantly atrial CMs from MSC-IPS1 cell lines (Male), $73.2\% \pm 7.7\%$ of total cells were atrial CMs (cTNT+ and MLC2V-), $n = 2$ batches. Differentiation cultures were dissociated to single cells for subsequent tissue seeding, as previously described (Zhang et al., 2016).

This study did not have large enough sample size to reach any conclusion on the influence of sex on the study outcome as 5 female and 1 male patient line was used in disease modeling. Thus, the sex analysis was not performed.

For authentication of cells that are expanded and differentiated in house, specifically C2A-CM, BJ1D iPSC, HES2 hESCs, HES3-NKX2-5^{eGFP/w} hESCs and cFB (see below), the samples were sent to the Genetic Analysis Facility, The Centre for Applied Genomics, The Hospital for Sick Children, Toronto, for Short Tandem Repeat (STR) profiling. The authentication information for commercial cell lines should be available from the manufacturer.

Primary Cultures

Human cardiac fibroblasts, cFBs, (Clonetics NHCF-V) were obtained from LONZA. The cells were cultured and passaged according to the manufacturer's protocol. Briefly, cFBs were thawed and cultured on 75cm² tissue culture flasks with FGM-3 Cardiac Fibroblast Growth Medium-3 BulletKit. Trypsin/EDTA (Life Technology) was used to detach cells during passaging. Passage 2-5 of cFB was used in the study.

Rat CMs (mixed genders) were isolated from neonatal rat (Sprague Dawley) hearts three days after birth as described (Zhang et al., 2016), according to a protocol approved by the University of Toronto Animal Care Committee.

METHOD DETAILS

Device Fabrication

Polystyrene sheet patterned with microwells

A repeating pattern consisting of rectangular microwells (5mm x 1mm x 300 μ m, L x W x H) interconnected by two parallel grooves (200 μ m x 100 μ m, W x H) was designed using AutoCAD. An SU-8 photoresist master mold was used to produce a negative

polydimethylsiloxane (PDMS) master mold (Zhang et al., 2016). The PDMS master was used to hot emboss the microwells into a polystyrene sheet (Figure S1A).

Polymer wires

Poly(octamethylene maleate (anhydride) citrate) (POMaC) polymer wires (100 μ m x 100 μ m, W x H) were prepared from a pre-polymer as previously described (Zhang et al., 2016). To fabricate the POMaC wires, a PDMS mold with parallel microchannels of the desired dimensions was fabricated from an SU-8 master, as previously described (Zhang et al., 2016). The PDMS mold was lightly pressed onto a glass slide and the POMaC pre-polymer solution was perfused through the microchannels by capillary action. The pre-polymer solution was then cured by UV exposure (5100 mJ/cm²). Due to the stronger adhesion of the POMaC wires to glass than PDMS, the POMaC wires remained adherent to the glass when the PDMS mold was carefully peeled off the glass slide. The POMaC wires were soaked in phosphate buffered saline (PBS) to release them from the glass slide and manually placed into the two parallel grooves patterned into the polystyrene sheet (Figure S1A). In some configurations, clear polyurethane 2-part adhesive (SP 1552-2, GS Polymers) was used in a minimal quantity to fix the POMaC wires in place (Domansky et al., 2013).

Hydrogel Preparation

Collagen hydrogel (500 μ L) was prepared by combining high concentration rat tail collagen (153 μ L at 9.82 mg/mL, Corning) with 15% (v/v) Matrigel (75 μ L, BD Biosciences), NaHCO₃ (50 μ L at 2.3 mM, Sigma), NaOH (5 μ L at 10 mM, Sigma), deionized sterile H₂O (167 μ L) and 1X M199 (50 μ L, Sigma) to result in a final collagen concentration of 3.0 mg/mL.

Electrical Stimulation Chamber Fabrication

Two $\frac{1}{8}$ inch-diameter carbon rods (Ladd Research Industries) were fixed 1 cm apart (inner edge-to-inner edge) to the bottom of a 10 cm tissue culture dish using polyurethane 2-part adhesive (Figure S1A). The carbon rods were connected to the lead wires of an external electrical stimulator (Grass Technology S88X Square Pulse Stimulator) with platinum wires (Ladd Research Industries).

Generation of Engineered Cardiac Tissues

Strips of polystyrene containing eight microwells were transferred to a 10 cm tissue culture dish (Figure S1A). The strip surface was rinsed with 5% (w/v) Pluronic Acid (Sigma-Aldrich) and then air-dried in the biosafety cabinet. Dissociated cardiac cells and cardiac fibroblasts (LONZA, Clonetics NHCF-V) were mixed in a 10:1 (ventricular cardiac cells: fibroblasts) or 10:1.5 (atrial cardiac cells: fibroblasts) cell number ratio, pelleted and resuspended at a concentration of 5.5×10^7 cells/mL (unless otherwise specified) in a hydrogel. This results in a 74,700 CMs per tissue on average. The cell-hydrogel suspension (2 μ L per well) was seeded into the polystyrene microwells, to give a final seeding concentration of 1.1×10^5 cells/microwell or 7.47×10^4 CMs/microwell. The tissues were cultured for 7 days to allow for remodeling and compaction around the POMaC wires. Daily bright field images of the tissues were taken using an Olympus CKX41 inverted microscope and CellSens software (Olympus Corporation). By Day 7, the tissues synchronously contracted and deflected the POMaC wire with each contraction.

To generate atrioventricular tissues, dissociated atrial cardiac cells and cardiac fibroblasts were mixed in a 10:1.5 cell number ratio. Dissociated ventricular cells and cardiac fibroblasts were mixed in a 10:1.5 cell number ratio. The mixed cells were pelleted and resuspended at a concentration of 5.75×10^7 cells/mL in collagen hydrogel. When seeding, cell-hydrogel mixture containing atrial CMs (1 μ L) was seeded on one side of the Biowire II well first, followed by a mixture containing ventricular CMs (1 μ L) seeded on the other side. After seeding, tissues were cultured for 7 days to allow for remodeling and compaction around the POMaC wires.

Electrical Stimulation Protocols

On Day 7, each strip of 8 tissues was transferred to an electrical stimulation chamber, such that the tissues were positioned between the carbon rods. On Day 7 and weekly thereafter, 4X bright field movies were taken of beating under stimulation at 1 Hz. The minimum voltage per cm required to stimulate the synchronized contraction of the tissue (excitation threshold, ET) and the maximum frequency the tissue could achieve in response to the stimulation pulse at twice the ET (maximum capture rate, MCR) were measured and recorded. POMaC is intrinsically fluorescent, hence the deflection of the polymer wire due to tissue contraction was isolated and tracked under the blue fluorescent light. Blue channel movies (10X objective; $\lambda_{\text{ex}} = 350$ nm, $\lambda_{\text{em}} = 470$ nm; 100 frames/s, 5 ms exposure) were taken to record the bending movement of the POMaC wire during tissue contraction from 1-3 Hz (1 Hz increase every 20 sec) to measure the force-frequency relationship (FFR). After testing for FFR, the tissue had been stimulated at high frequency (6 Hz) for 20 sec; stimulation was then turned off and re-initiated at 1 Hz to measure the post-rest potentiation (PRP) of the force. To quantify the FFR and PRP, all measurements were normalized to the 1 Hz baseline values. All imaging was performed using an Olympus IX81 inverted fluorescent microscope and CellSens software (Olympus Corporation).

The Day 7 electrical excitability assessments were used to determine the long-term stimulation conditions, specifically stimulation voltage (1.5-times the ET_{avg}). Electrical stimulation was continued with weekly monitoring of ET, MCR, FFR, and PRP. Culture media was changed every week.

Electrical stimulation protocol of weekly 1 Hz increase in frequency was implemented for ventricular maturation. If average MCR exceeded 4 Hz after one week of 2 Hz stimulation or exceeded 5 Hz after one week of 3 Hz stimulation, stimulation frequency can be changed directly from 2 Hz to 4 Hz or 3 Hz to 5 Hz to accelerate the process. End point assessments were performed when a positive FFR in the range from 1 to 3 Hz was achieved. If a positive FFR was not observed once the frequency reached 6 Hz, stimulation

continued at 6 Hz, until a positive FFR was observed. The stimulation voltage was adjusted weekly to 1.5-times the average ET, down to a minimum voltage of 3.5 V/cm. For atrial preparations, a similar procedure was applied with the daily increase of the stimulation frequency by 0.4 Hz, from 2 Hz to 6 Hz, then retaining the stimulation frequency at 6 Hz for 1 week.

For the ventricular disease model preparation, the experimentalists were blinded to the study groups. Tissues were generated from the non-affected A, non-affected B, non-affected C, affected D, affected E, and affected F CMs. Electrical stimulation started at 2 Hz on day 7 post cell seeding and the protocol of 1 Hz weekly step-up was used until the frequency reached 6 Hz, at which point it was maintained at 6 Hz for one week. Subsequently, the frequency was decreased to 3 Hz and maintained at that level for the remainder of the cultivation period, up to 6 months. Tissues were assessed after 6 weeks and 8 months of culture.

For atrioventricular preparations, electrical stimulation started at 2 Hz on day 7 after seeding and the protocol of 1 Hz weekly step-up was used until the frequency reached 6 Hz. If average MCR exceeded 4 Hz after one week of 2 Hz stimulation, or exceeded 5 Hz after one week of 3 Hz stimulation, stimulation frequency could be changed directly from 2 Hz to 4 Hz or 3 Hz to 5 Hz to accelerate the process. The stimulation at 6 Hz was maintained for 1 week, at which point it was decreased to 3 Hz and maintained for a period of several days until the tissues were used for drug testing.

Atrial and Ventricular Tissue RNA Sequencing

RNA was isolated using a commercially available kit: PicoPure RNA Isolation Kit (Thermo Fisher, KIT0204) and RNase-Free DNase Set (QIAGEN #79254). RNA sequencing was performed at the Illumina CPro Next Generation Sequencing facility of the Donnelly Sequencing Centre at the University of Toronto. Alignments were made using the pseudo alignment method from Kallisto (Bray et al., 2016). The transcriptome used was obtained from ESEMBL, human genome build GRCh38.p10, yielding 63967 genes and over 200,000 spliced transcripts. Single end mode with a mean fragment insert size of 270 and SD of 40 bases was used. Counts were quantified from Kallisto output files using Sleuth (Pimentel et al., 2017). Technical and biological variance was calculated using Sleuth to yield test statistics based on a linear model, where the treatment was corrected against the intercept. No batch was present in the dataset as all samples were sequenced across 4 flow cells to generate approximately 20 million reads per sample. Log fold changes were calculated using DESeq2. Heatmaps were generated using the R function *pheatmap*.

Gene set enrichment analysis

Normalized counts of RNA-sequencing data were processed using the R function *voom* to transform counts into Gaussian distributions. The R function *camera* was used to calculate gene set enrichments to the Gene Ontology Biological Process gene sets obtained from the Broad Institute and custom ontology files generated from differential expression analysis using the R library *limma* of deposited human atrial and ventricle gene expression data (GSE2240). The gene matrix table file for gene set enrichment of atria and ventricle gene expression data was generated using custom R scripts. Output from *camera* gene set enrichment analysis was formatted as a generic table format for graphing and analysis in Cytoscape using custom R scripts. Network graphs of gene set enrichments were generated in Cytoscape using *enrichmentmap*. Sub-networks were named using *clustermaker* and word cloud annotating for enrich words with a bonus for adjacent words.

Gene Expression for Patient Derived Cells

Gene expression of ventricular tissues based on individual hiPSC-CM cell lines (affected D, E, and F and non-affected A, B, and C) at the end of 8 month cultivation with electrical conditioning, was assessed as previously described (Aggarwal et al., 2014). Whole transcriptome sequencing was done utilizing the Ion Total RNA-Seq Kit and the Ion Torrent Proton System (ThermoFisher Scientific) following manufacturer's recommendations. Data analysis was performed using QIAGEN's Ingenuity Pathway Analysis (IPA) software with the overlay tool IPA-Tox. The feature "Tox List" was set at default parameters to analyze genes contributing to principle component analysis between affected D, E, and F and non-affected A, B, and C, focusing on cardiotoxicity.

Elastic Modulus of Polymer Wires

To determine the elastic modulus of the POMaC wires, testing strips (1.5 mm x 10 mm x 0.1 mm) were cured at 5100 mJ/mm², the same condition used for preparation of Biowire II platform. The tensile test was conducted with a Myograph (Kent Scientific) in the longitudinal direction of strips ($n \geq 3$), using a modified ASTM D638-10 Standard Test Method for Tensile Properties of Plastics as described (Zhang et al., 2016).

To test the long-term POMaC wire stability, the testing strips were placed in a 12-well plate in media (DMEM, 10% fetal bovine serum (FBS), 1% Penicillin-Streptomycin). A transwell insert (Corning) seeded with 1×10^5 neonatal rat CMs, isolated as described above, was added to each well. Media was changed twice a week and mechanical tests were performed on Day 0, 15, 30, 60 and 90.

Polymer Wire Force-Displacement Curves

The force required to displace the POMaC wire was determined using a microscale mechanical tester, MicroSquisher (CellScale). The 0.1524 mm diameter tungsten probe was modified with custom tips (0.5 mm, 0.7 mm, and 0.8 mm diameter) to recapitulate the tissue diameter and curvature on the POMaC wire. The custom tips (half ellipse, 4:1 diameter ratio) were fabricated from an SU-8 master by soft lithography and attached to the tungsten probe using an adhesive (T-GSG-01 Titan Gel). Four separate

8-well polystyrene strips with POMaC wires were tested per probe tip. The polystyrene strips were soaked in media for 7 days prior to testing. During the test, the polystyrene strip was affixed to a 10 cm Petri dish and testing was performed in culture media. The probe tip was placed at one end of microwell and moved toward the POMaC wire at a velocity of 2.5 $\mu\text{m/s}$. The tip displaced the wire at the midsection, applying the force perpendicular to the long axis of the POMaC wire. The force, probe displacement (0–150 μm) and time were recorded ($n \geq 55$). The experimental data, over the entire range, for each custom tip were fit to a third-degree polynomial equation, generating a force-displacement calibration curve for each custom probe tip (Figure S1E).

To assess if cell cultivation around the polymer wire affects the force-displacement curve, a batch of polystyrene chips with POMaC wires were fabricated and divided into two groups. Both groups were incubated in media at 37°C for a week before use. Group one was tested right after the incubation as described above, whereas group two was tested after cell seeding and approximately two months of ventricular tissue conditioning. A probe tip of 0.5 mm was used during the tests. Fitted curves, 95% confidence interval curves, and R^2 values were calculated with Prism 6.0.

Finite Element Modeling (FEM)

The finite element model simulated the behavior of the POMaC wires during mechanical testing. The model included the polymer wire and the indenter; the dimensions and material properties for the FEM components were set to match the conditions during experimental testing. The two ends were constrained by fixed supports and the load was applied to the polymer wire through the indenter. The mesh was made of solid elements, and the number of elements and mesh nodes in the model for the 0.5 mm indenter were 11448 and 52622, for the 0.7 mm indenter were 15702 and 71225, and for the 0.8 mm indenter were 18468 and 83232, respectively. A neo-Hookean, hyperelastic material model was used for the POMaC material to account for the non-linear behavior and the large deformations observed during physical testing. Poisson ratio was assumed to be 0.5.

Active and Passive Force for Cardiac Tissues

Blue channel image sequences were analyzed using a custom MATLAB code that traced the maximum deflection of the POMaC wire. Average tissue width (diameter) and width of the tissue on the polymer wire (T_w) were measured from still frames of the 4X bright field video of the tissue in the relaxed position (Figures S1C and S1D). Total (at peak contraction) and passive (at rest) POMaC wire deflections were converted to force measurements (μN) using the force calibration curves described in the previous section. The final readouts for the total and passive tension of tissue were then interpolated according to the T_w and custom tip sizes. The active force was calculated as the difference between the total and passive tension. (Figure 2C). The custom MATLAB code was used to calculate the passive tension, active force, contraction and relaxation duration, and upstroke and relaxation velocity.

Absorption Testing

For the acute test, polystyrene strips containing microwells and POMaC wires, with and without the adhesive, were cut into chips (9mm x 9mm x 1mm) containing a single microwell. Chips of the same geometry were also made with PDMS. The polystyrene and PDMS chips were incubated in 650 μL Rhodamine 6G (10nM; Sigma-Aldrich) in closed round bottom polypropylene test tubes at room temperature for half an hour. Rhodamine 6G solution without any chip incubating at same condition was used as a control. 200 μL of the dye solution was transferred to a 96-well plate and the fluorescence was read using a SpectraMax i3 plate reader (Molecular Devices; $\lambda_{\text{ex}} = 526\text{nm}$, $\lambda_{\text{em}} = 555\text{nm}$), ($n = 12$).

For the long-term absorption test, polystyrene strips containing microwells and POMaC wires, with and without the adhesive, were cut into chips (9mm x 9mm x 1mm) containing a single microwell. Chips of the same geometry were also made using PDMS. The polystyrene and PDMS chips were incubated in 1mL Rhodamine B (1 μM ; Sigma-Aldrich) in a 24 well-plate at 37°C for up to 1 week. Tissue culture treated 24 well plates were incubated with the dye in the absence of any chips as a control. At 6 h, 24 h, 48 h, and 1 week, 100 μL of the dye solution was transferred to a 96-well plate and the fluorescence was read using a SpectraMax i3 plate reader (Molecular Devices; $\lambda_{\text{ex}} = 540\text{ nm}$, $\lambda_{\text{em}} = 625\text{ nm}$), ($n = 3$). Additionally, fluorescent images of the chips were taken in the absence of treatment, after 1 week of dye incubation, and after 2 h of washing following 1 week of dye incubation.

Immunostaining and Confocal Microscopy

Tissues were fixed with 4% paraformaldehyde, permeabilized with 0.2% Tween 20, and blocked with 10% FBS. Immunostaining was performed using the following primary antibodies: mouse anti-cardiac Troponin T (cTnT) (ThermoFisher; 1:200), rabbit anti-Connexin 43 (Cx-43) (Abcam; 1:200), mouse anti- α -actinin (Abcam; 1:200), rabbit anti-myosin light chain-2v (Santa Cruz; 1:200), goat anti-caveolin3 (Santa Cruz; 1:100); and the following secondary antibodies: donkey anti-mouse-Alexa Fluor 488 (Abcam; 1:400), donkey anti-rabbit-Alexa Fluor 594 (Abcam; 1:200) and donkey anti-goat-Alexa Fluor 647 (Life Technologies; 1:200). Phalloidin-Alexa Fluor 660 (Invitrogen; 1:200) was used to stain F-actin fibers. Conjugated vimentin-Cy3 (Sigma; 1:200) was used to stain for vimentin. Confocal microscopy images were obtained using an Olympus FluoView 1000 laser scanning confocal microscope (Olympus Corporation).

Live and dead staining was performed with CFDA (1:1000, Life Technologies) and Propidium Iodide (75:1000, Life Technologies) in PBS. Viability was calculated as the average intensity of CFDA divided by the sum of average intensities of CFDA and PI. ($n \geq 3$)

Sarcomere presence was quantified by average intensity of α -actinin divided by the average intensity of DAPI counterstain. ($n = 3$)

Transmission Electron Microscopy

The tissues were fixed with 4% paraformaldehyde, 1% glutaraldehyde in PBS for at least overnight and washed 3-times with PBS. Secondary-fixation was done with 1% osmium tetroxide in PBS for 1 hr. The tissues were dehydrated using an ethanol series from 50% to 100%. Tissues were infiltrated using Epoxy resin and polymerized in plastic dishes at 40°C for 48h. The tissues were stained with uranyl acetate and lead citrate after sectioning. Imaging was performed using a Hitachi H-7000 transmission electron microscope (Hitachi) in Microscopy Imaging Laboratory, Faculty of Medicine, University of Toronto.

Contractile and Ca^{2+} Transients

To investigate the contractile effects of various compounds on the tissues, a custom testing chamber was fabricated in a 6-well plate modified with an extraction/injection port connected to a 5mL syringe, a pair of carbon electrodes (set 1cm apart) with platinum wire lead attachments and a custom 3D-printed holder for a polystyrene chip with a single microwell. Prior to testing, the tissue was transferred to the custom testing chamber and placed in the environmental chamber on the microscope stage (37°C, 5% CO_2), where it was allowed to equilibrate for 30 min in the presence of electrical field stimulation (1Hz, at ET). A bright field video of the tissue was taken before testing to obtain all the necessary measurements for the force calculation. For testing, the voltage was increased to 10% above the ET, and videos were taken of one polymer wire (10X objective). Prior to the test compound injection, media were extracted and injected through the port twice at 10 min intervals to pre-condition the tissue to the testing process. Compounds were diluted in media at concentrations 1000-fold higher than the desired final concentration. For compound testing, 1/3rd of the media was extracted from the chamber, the compound was added to the extracted media and then slowly injected back into the testing chamber. After 10-15min, videos in the blue channel were recorded. The procedure was repeated for sequential drug dosages. The videos were analyzed using the custom MATLAB software, as indicated for the weekly FFR assessments.

To investigate the relative changes of intracellular Ca^{2+} concentration, tissues were incubated with the Ca^{2+} dye fluo-4 NW (Thermo Fisher) for 30 min at 37 °C prior to testing. To obtain both Ca^{2+} transients and contractility readouts consecutively and synchronously, the testing process was performed using both green light channel ($\lambda_{\text{ex}} = 490 \text{ nm}$, $\lambda_{\text{em}} = 525 \text{ nm}$) and/or blue channel at 10X or 4X magnification. The ImageJ software (NIH) Stacks plugin was used to determine the average intensity of a region of interest in the tissue located at a distance from the POMaC wire, wherein the movement artifacts were minimal. The ratio of peak tissue fluorescence intensity to baseline intensity, dF/F_0 was calculated to determine the relative changes in intracellular Ca^{2+} in the presence of the compound. For the consecutive force and Ca^{2+} transient readouts, contractile measurements were extracted from the blue channel as described before. For the synchronous readouts, the contractile measurements were extracted from the green channel videos using modified version of the ImageJ SpotTracker plugin. Prism 6.0 was used to calculate the IC_{50} .

Intracellular Recordings

Tissues were perfused with 35-37°C Krebs's Solution (118mM NaCl, 4.2mM KCl, 1.2mM KH_2PO_4 , 1.2mM MgSO_4 , 1.8mM CaCl_2 , 23mM NaHCO_3 , 2mM Na-pyruvate and 20mM glucose, equilibrated with 95% O_2 and 5% CO_2 ; pH 7.4) or DMEM medium. They were paced at twice the ET. The APs were recorded with high impedance microelectrodes (60-90M Ω) filled with 3M KCl, connected to an Axopatch 200B amplifier (Axon Instruments). Recordings were performed in current clamp mode at 2kHz and signals were analyzed using the Clampfit 10 Data Analysis Module of the pCLAMP 10 Electrophysiology Data Acquisition & Analysis Software (Axon Instruments). The movement of the tissue was minimized by perfusing with 10 μM blebbistatin (Toronto Research Chemicals) for 20min. The effect of various compounds on the AP was assessed by preparing an appropriate dilution of the compound in Krebs's Solution or DMEM.

Optical Mapping

Tissues were perfused with 5 μM voltage-sensitive dye, Di-4-ANEPPS (Invitrogen), in Krebs's Solution at 35-37 °C for 20min. Dye fluorescence was recorded on an MVX-10 Olympus fluorescence microscope (Olympus Corporation) equipped with a charged coupled device (CCD) (Cascade 128, Photometrics). The 1cm sensor had 128 × 128 pixel resolution. Recordings were performed at 500 frames/s with 0 exposure time. Biowires were paced at 1.5-2 Hz with a Pulsar 6i Stimulator (FHC) at twice the ET.

QUANTIFICATION AND STATISTICAL ANALYSIS

Statistical analysis was performed using Prism 6.0 and SigmaPlot 12.0. All data are represented as mean \pm standard derivation (SD) or standard errors of mean (SEM), which have been indicated in each figure. Indicated sample sizes (n) represent individual tissue samples. For intracellular recordings, sample size (n) represents the number of cells analyzed from three or more independent experiments. No statistical method was used to predetermine the samples size. Disease modeling was conducted in a blinded fashion. Differences between experimental groups were analyzed by Student's t test, Welch's t-test or Mann Whitney test (two groups) and one-way ANOVA or ANOVA on ranks (more than two groups). Experiments with two different variables were analyzed with two-way ANOVA. Normality test (Shapiro-Wilk, D'Agostino & Pearson omnibus or Kolmogorov-Smirnov test with Lilliefors) and pairwise multiple comparison procedures (Tukey's post hoc method or Holm-Sidak method or Sidak-Bonferroni method or Dunnett's method or Dunn's method) were used. $p < 0.05$ was considered significant for all statistical tests.

DATA AND SOFTWARE AVAILABILITY

The RNA sequencing data have been archived at the short read archive at NCBI. The accession number for the RNA sequencing data for atrial and ventricular tissues is NCBI: GSE114976 (<https://www.ncbi.nlm.nih.gov/geo/query/acc.cgi?acc=GSE114976>) and for the disease models it is NCBI: GSE122661 (<https://www.ncbi.nlm.nih.gov/geo/query/acc.cgi?acc=GSE122661>). Other information and requests for data and software may be directed to, and will be fulfilled by the Lead Contact, Milica Radisic (m.radisic@utoronto.ca).

Supplemental Figures

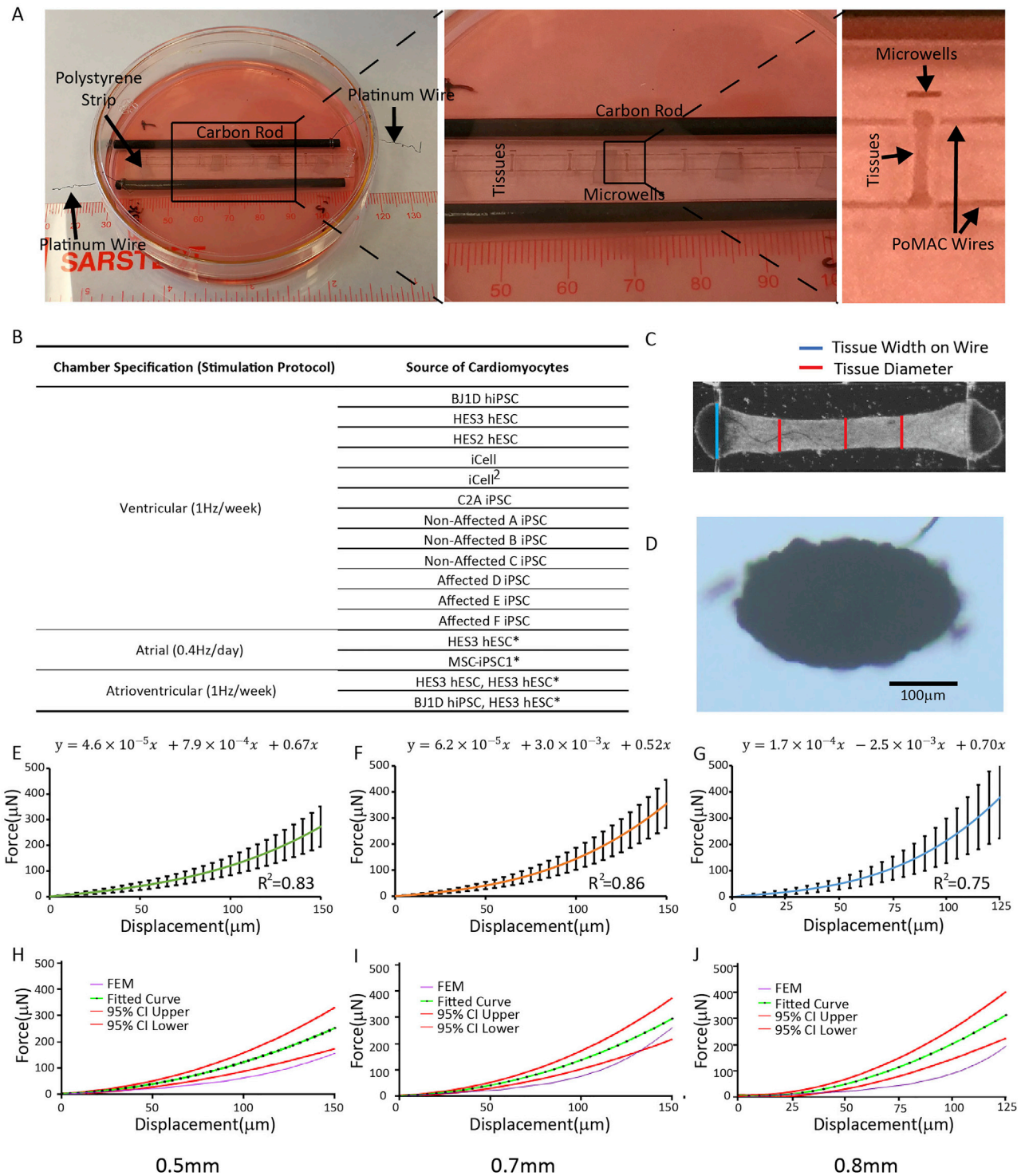


Figure S1. Experimental Setup and Force-Displacement Curves for POMaC Wires, Related to Figures 1 and 2

(A) A Petri-dish is fitted with a pair of carbon electrodes and a polystyrene strip for cultivation of eight cardiac tissues. Position of tissues and polymer wires with respect to carbon electrodes is indicated in the zoomed-in images.

(B) Summary of experimental conditions, *denotes the preparation for atrial differentiation.

(C) Measurements of tissue width on the POMaC wire and the tissue diameter. Average tissue diameter is determined from multiple locations.

(legend continued on next page)

(D) The representative image of cross-section from a tissue, scale bar, 100 μm . Force-displacement curves for the POMaC wire obtained by microscale mechanical testing using custom (E) 0.5 mm, (F) 0.7 mm, and (G) 0.8mm diameter probes.

(E–G) Polynomial equation fit and R^2 to the experimental data (data presented as mean \pm stdev, $n \geq 55$).

(H–J) Finite element model of the polymer wire force-displacement behavior using a neo-Hookean model (purple lines) compared to the experimental data illustrated by the average values (green lines) and 95% confidence intervals (red lines).

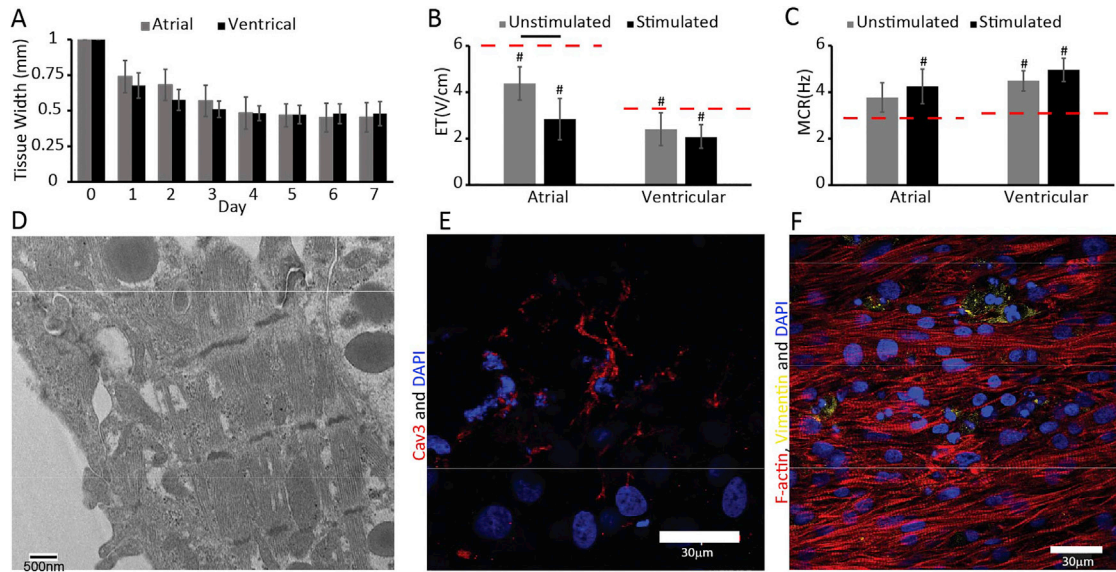


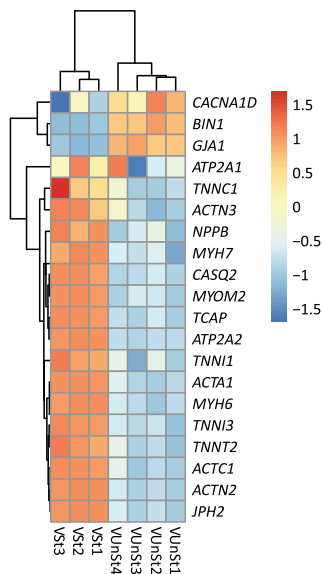
Figure S2. Tissue Compaction, Electrical Excitability Properties, and Structural Characterization, Related to Figures 3 and 4

(A) Atrial and ventricular tissues compact in a similar fashion in the first week after seeding. ($n \geq 8$).

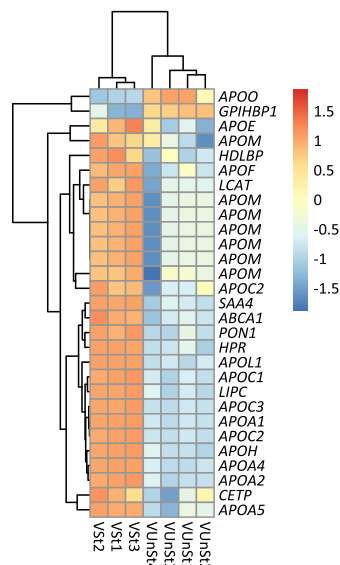
(B and C) (B) Excitation Threshold (ET); (C) Maximum Capture Rate (MCR), for unstimulated and stimulated atrial and ventricular tissues. All data presented as mean \pm stdev, $n \geq 8$. Red dashed lines represent the average ET and MCR at day 7 after tissue compaction. # denotes significant differences compared to day 7. Atrial tissues were derived from HES3 ESC-CM and ventricular from BJ1D iPSC-CM.

(D–F) (D) Representative TEM image of a stimulated ventricular tissue generated from BJ1D hiPSC-CMs; Scale bar, 500 nm. Representative confocal image of (E) a stimulated ventricular tissue generated from C2A hiPSC-CMs immunostained for caveolin 3 and counterstained with the nuclear stain DAPI, and (F) a stimulated ventricular tissue generated from BJ1D hiPSC-CMs immunostained for vimentin, F-actin and counterstained with DAPI; Scale bar, 30 μ m.

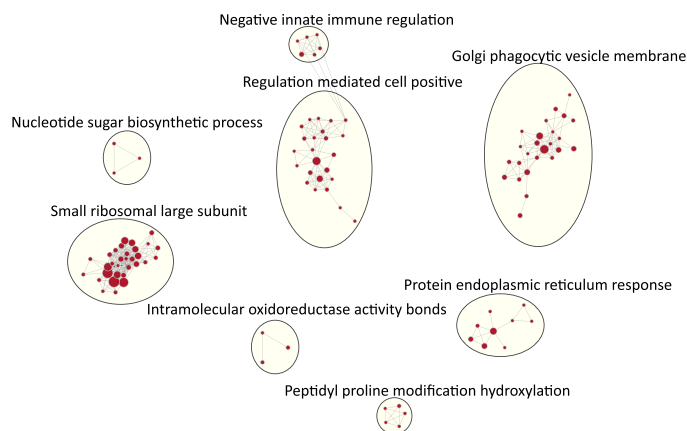
A



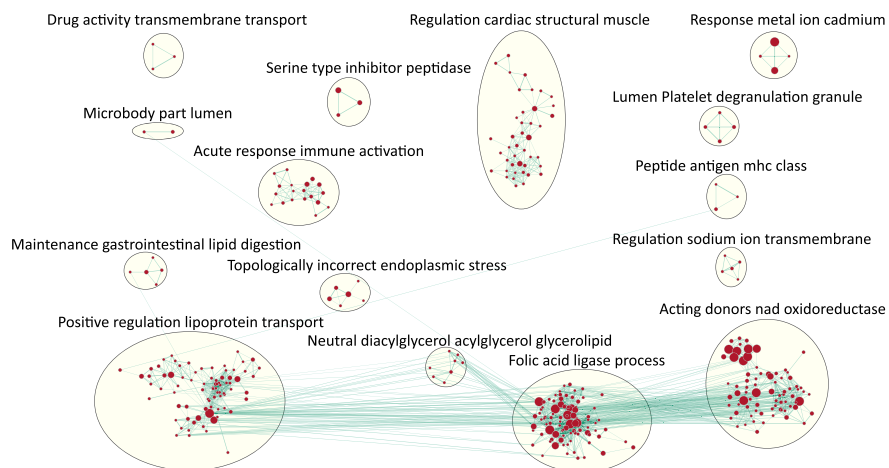
B



C



D



(legend on next page)

Figure S3. Gene Expression Analysis of Atrial and Ventricular Tissues with and without Electrical Conditioning, Related to Figures 3 and 4

(A) Differential expressions of selected ventricular maturation markers.

(B) Electrical conditioning significantly enhances expression of genes related to high density lipoprotein (HDL) metabolism in ventricular tissues. Network graph representation of enriched ontologies annotated for sub-networks.

(C) Gene ontologies (biological process) that were significantly upregulated with electrical conditioning in atrial biowires.

(D) Gene ontologies (biological process) that were significantly upregulated with electrical conditioning in ventricular biowires. Atrial and ventricular tissues were created from HES3 hESC-CM.

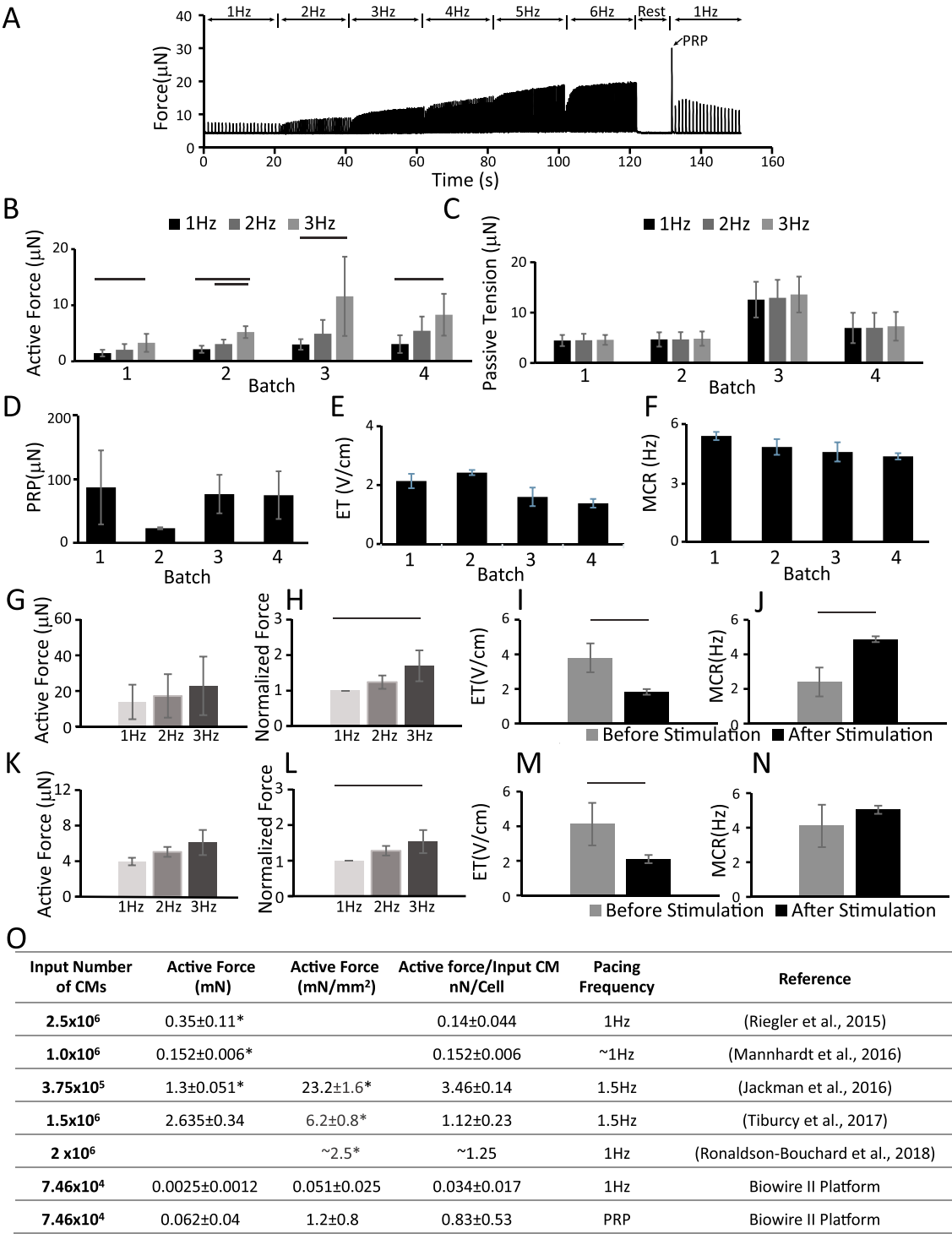


Figure S4. Batch-to-Batch Variability, Cell Line Variability, and Comparison of Active Forces Achieved by Ventricular Tissues, Related to Figure 4

Consistency of ventricular tissues generated from four batches of BJ1D hiPSC-CMs.

(A) A representative trace of an FFR and PRP test.

(B) Active force (one way ANOVA with Tukey's multiple comparisons test).

(legend continued on next page)

(C–N) (C) Passive tension from 1 to 3Hz, (D) Post-Rest Potentiation (PRP), (E) Excitation Threshold (ET), and (F) Maximum Capture Rate (MCR). Data presented as mean \pm stdev, ($n \geq 4$ tissues per experiment). After applying maturation protocol, electrical function was improved for ventricular tissues derived from (G–J) HES2 and (K–N) HES3 cell lines in terms of (G) and (K) active force from 1 to 3Hz; (H) and (L), normalized active force from 1 to 3Hz; (I) and (M), excitation Threshold (ET); and (J) and (N), maximum Capture Rate (MCR); (Data presented as mean \pm stdev, $n \geq 3$, One-way ANOVA or ANOVA on ranks or Student's t test). (O) Summary of active forces achieved by engineered cardiac tissues derived from human CMs in other publications.

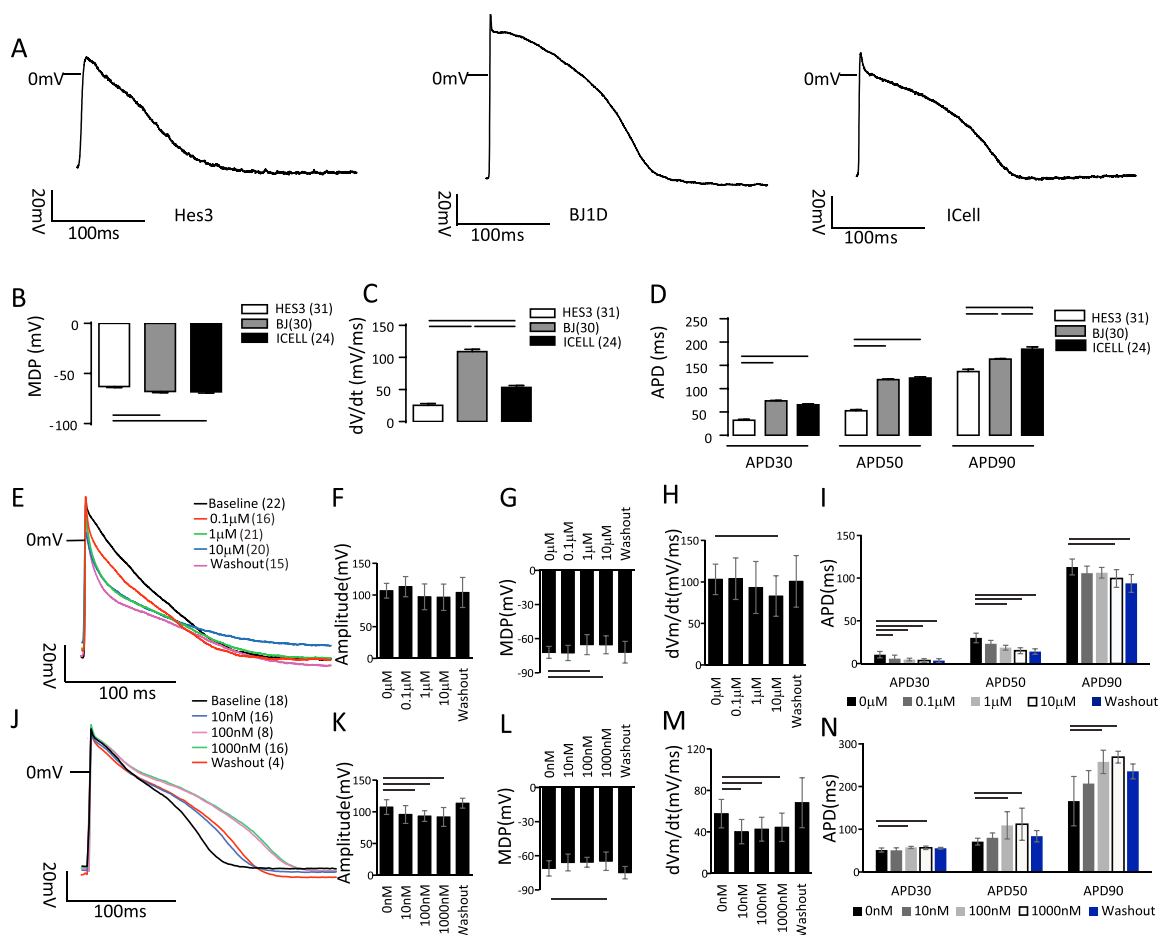


Figure S5. AP Characterization of Ventricular Tissues Generated from Different Cell Lines and Responses of BJ1D Ventricular Tissues to Verapamil and Dofetilide, Related to Figure 4

(A) CMs derived from HES3, BJ1D and iCell cell lines were assessed with sharp microelectrode recordings performed at the end of cultivation and exhibited some differences in AP profiles. Traces show HES3, BJ1D and iCell derived CMs AP profiles respectively. 90% of BJ1D CMs and 39% of iCell CMs had a notch in their AP profiles.

(B–D) (B) Minimum diastolic potential and (C) Upstroke velocity. AP duration at (D) 30% repolarization (APD₃₀), 50% repolarization (APD₅₀) and 90% repolarization (APD₉₀). Data presented as mean ± SEM, n ≥ 3 tissue, One-way ANOVA with Tukey post hoc multiple comparison test or ANOVA on ranks. Numbers in brackets indicate the total number of individual cells sampled. (E–N) Ventricular tissues (derived from BJ1D hiPSC-CMs) treated with (E–I) verapamil and (J–N) dofetilide. (E and J) Representative AP recordings. (F and K) AP amplitude. (G and L) Minimum diastolic potential. (H and M) Upstroke velocity and (I and N) APD₃₀, APD₅₀, and APD₉₀.

Data presented as mean ± SEM, n = 3 tissue, One-way ANOVA with Dunnett's multiple comparison of test concentrations to 0 μM or ANOVA on ranks. Numbers in brackets indicate the total number of individual cells sampled at each concentration.

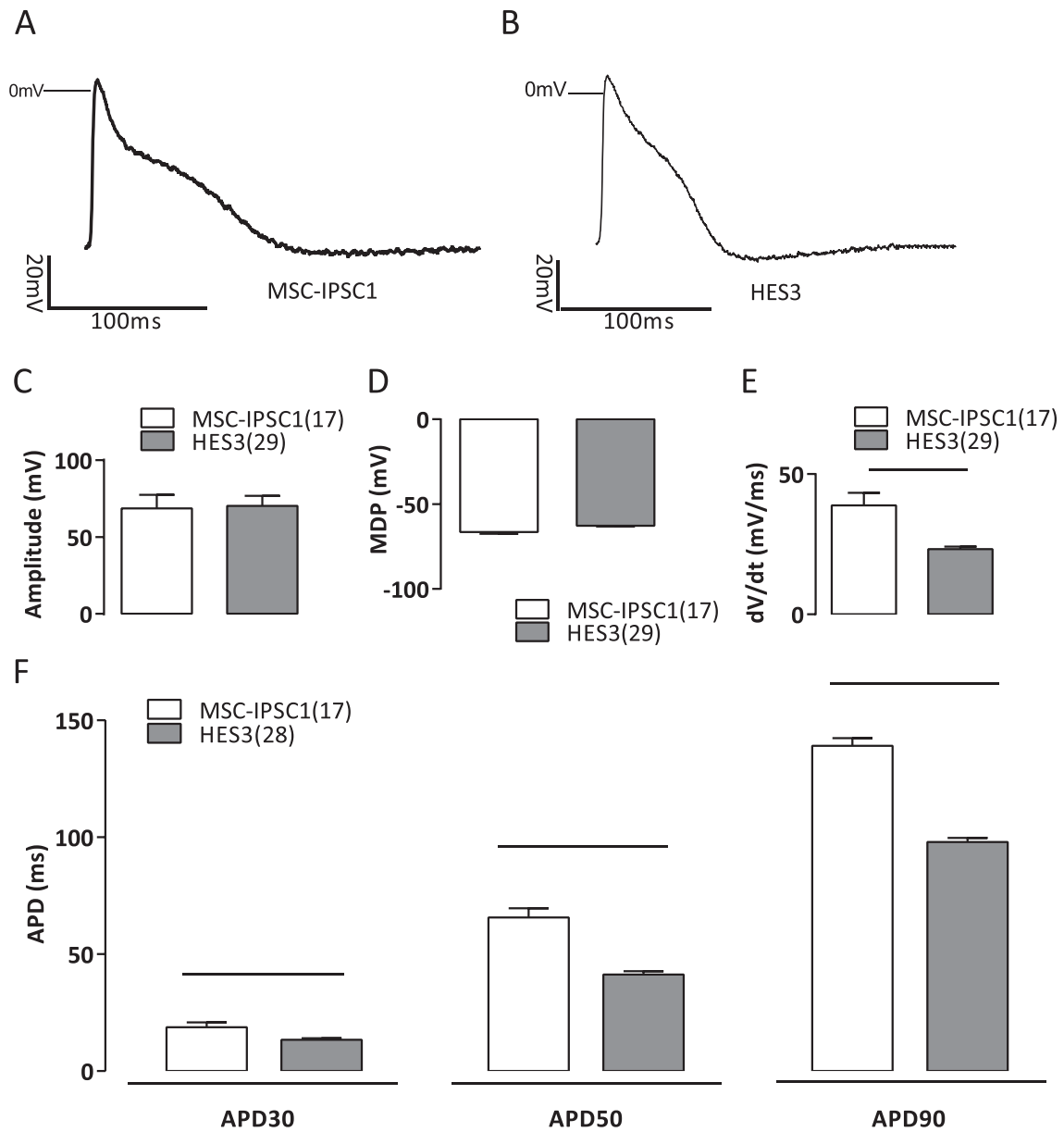


Figure S6. AP Characterization of Atrial Tissues Generated from Two Different Cell Lines, Related to Figure 4

(A–F) MSC-IPSC1 (A) and HES3 (B) cell lines were assessed with sharp microelectrode recordings at the end of cultivation and exhibited some differences in AP profiles, (C) AP amplitude, (D) Minimum diastolic potential, (E) Upstroke velocity, and (F) AP duration at 30% repolarization (APD₃₀), 50% repolarization (APD₅₀) and 90% repolarization (APD₉₀). Numbers in brackets indicate the total number of individual cells sampled.

Data presented as mean ± SEM, $n \geq 4$ tissue, Student's or Welch's t-test.

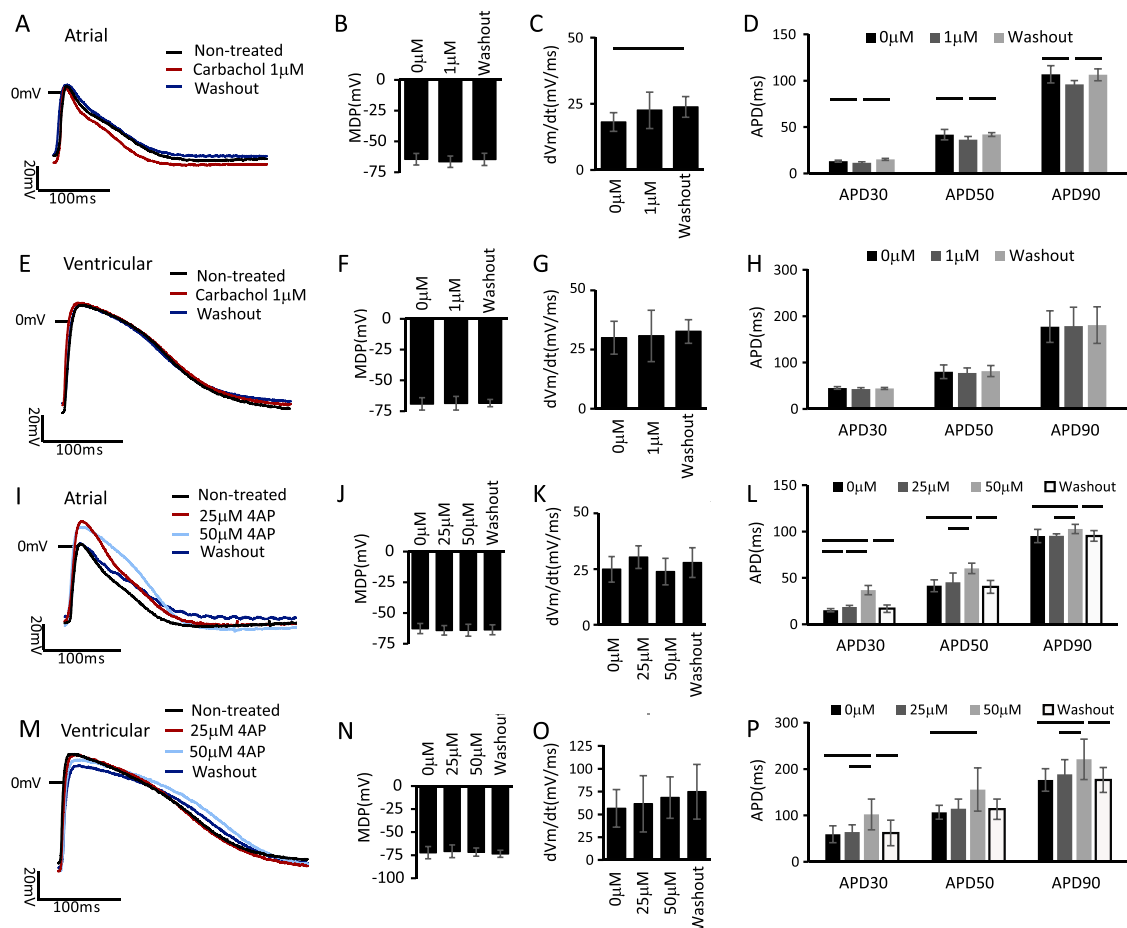


Figure S7. Atrial and Ventricular Tissues Exhibit Chamber Specific Electrophysiological Responses to Drugs, Related to Figure 4

(A) Representative AP of an atrial tissue treated with carbachol.

(B–D) Quantification of (B) minimum diastolic potential, (C) upstroke velocity, (D) duration to 30% repolarization (APD₃₀), to 50% repolarization (APD₅₀) and to 90% repolarization (APD₉₀), for atrial tissues treated with carbachol. (mean \pm stdev, $n \geq 3$, one way ANOVA or ANOVA on ranks).

(E) Representative AP of a ventricular tissue treated with carbachol.

(F–H) Quantification of the (F) minimum diastolic potential, (G) upstroke velocity, (H) APD₃₀, APD₅₀ and APD₉₀, for ventricular tissues treated with carbachol. (mean \pm stdev, $n \geq 3$, one way ANOVA or ANOVA on ranks).

(I) Representative AP of an atrial tissue treated with 4-aminopyridine (4AP).

(J–L) Quantification of the (J) minimum diastolic potential, (K) upstroke velocity, (L) APD₃₀, APD₅₀ and APD₉₀, for atrial tissues treated with 4AP. (mean \pm stdev, $n \geq 3$, one way ANOVA or ANOVA on ranks).

(M) Representative AP of a ventricular tissue treated with 4AP.

(N–P) Quantification of the (N) minimum diastolic potential, (O) upstroke velocity, (P) APD₃₀, APD₅₀ and APD₉₀, for ventricular tissues treated with 4AP. (mean \pm stdev, $n \geq 3$, one way ANOVA, or ANOVA on ranks). Atrial tissues were derived from HES3 hESC-CM and ventricular from BJ1D iPSC-CM.